

Neural-Rendezvous: Learning-based Robust Guidance and Control to Encounter Interstellar Objects*

Hiroyasu Tsukamoto [†] and Soon-Jo Chung [‡]

Graduate Aerospace Laboratories, California Institute of Technology, Pasadena, CA, 91125, USA

Benjamin Donitz[§], Michel Ingham[¶], Declan Mages^{||}, Yashwanth Kumar Nakka^{**}

Jet Propulsion Laboratory, California Institute of Technology, Pasadena, CA, 91109, USA

Interstellar objects (ISOs), astronomical objects not gravitationally bound to the Sun, are likely representatives of primitive materials invaluable in understanding exoplanetary star systems. Due to their poorly constrained orbits with generally high inclinations and relative velocities, however, exploring ISOs with conventional human-in-the-loop approaches is significantly challenging. This paper presents Neural-Rendezvous – a deep learning-based guidance and control framework for encountering any fast-moving objects, including ISOs, robustly, accurately, and autonomously in real-time. It uses pointwise minimum norm tracking control on top of a guidance policy modeled by a spectrally-normalized deep neural network, where its hyperparameters are tuned with a newly introduced loss function directly penalizing the state trajectory tracking error. We rigorously show that, even in the challenging case of ISO exploration, Neural-Rendezvous provides 1) a high probability exponential bound on the expected spacecraft delivery error; and 2) a finite optimality gap with respect to the solution of model predictive control, both of which are indispensable especially for such a critical space mission. In numerical simulations, Neural-Rendezvous is demonstrated to achieve a terminal-time delivery error of less than 0.2 km for 99% of the ISO candidates with realistic state uncertainty, whilst retaining computational efficiency sufficient for real-time implementation.

Nomenclature

\mathcal{A}	= weak infinitesimal operator of stochastic processes
C_{s2v}	= matrix that maps x to \dot{p} , i.e., $C_{s2v} = [O_{3 \times 3} \ I_{3 \times 3}] \in \mathbb{R}^{3 \times 6}$
\mathbb{E}	= expected value operator

*Submitted to AIAA Journal of Guidance, Control, and Dynamics (YouTube video: <https://youtu.be/60tTkmw1tIY>)

[†]Ph.D. Student, Department of Aerospace, Student Member AIAA.

[‡]Bren Professor of Aerospace and Control and Dynamical Systems and JPL Senior Research Scientist, Associate Fellow AIAA.

[§]Systems Engineer, Advanced Systems Design Engineering Group, Member AIAA.

[¶]Chief Technologist, Flight Software Systems Engineering and Architectures Group, Associate Fellow AIAA.

^{||}Navigation Engineer, Outer Planet Navigation Group.

^{**}Postdoctoral Scholar, Maritime and Multi-Agent Autonomy Group, Member AIAA.

\mathbb{E}_Z	=	conditional expected value operator given Z
$\mathbf{I}_{m \times n}$	=	$m \times n$ identity matrix
L_ℓ	=	2-norm Lipschitz constant of u_ℓ
m	=	dimension of spacecraft control input ($= 3$)
$m_{\text{sc}}(t)$	=	mass of spacecraft at time t
\mathbb{N}	=	set of natural numbers
N_d	=	number of neural network training samples
n	=	dimension of spacecraft and ISO state ($= 6$)
$\mathbf{O}_{m \times n}$	=	$m \times n$ zero matrix
$\alpha(t), \hat{\alpha}(t), \alpha_d(t)$	=	true, estimated, and desired orbital elements of ISO at time t
\mathbb{P}	=	probability measure
$p(t), \hat{p}(t), p_d(t)$	=	true, estimated, and desired position of spacecraft relative to ISO in LVLH frame at time t
\mathbb{R}	=	set of real numbers
$\mathbb{R}_{>0}$	=	set of positive real numbers
$\mathbb{R}_{\geq 0}$	=	set of non-negative real numbers
$x(t), \hat{x}(t), x_d(t)$	=	true, estimated, and desired state of spacecraft relative to ISO in LVLH frame at time t
t	=	time
t_d	=	time to compute desired state trajectory
t_f	=	terminal time at ISO encounter
t_s	=	time to activate u_ℓ^*
$\mathcal{U}(t)$	=	set containing admissible control input at time t
u	=	control policy
u_ℓ	=	SN-DNN guidance policy
u_ℓ^*	=	SN-DNN min-norm control policy
u_{max}	=	maximum admissible control input
u_{mpc}	=	MPC policy
$y(t)$	=	state measurement at time t
θ_{nn}	=	hyperparameter of u_ℓ
ρ	=	desired terminal position of spacecraft relative to ISO

Acronyms

DNN	=	deep neural network
-----	---	---------------------

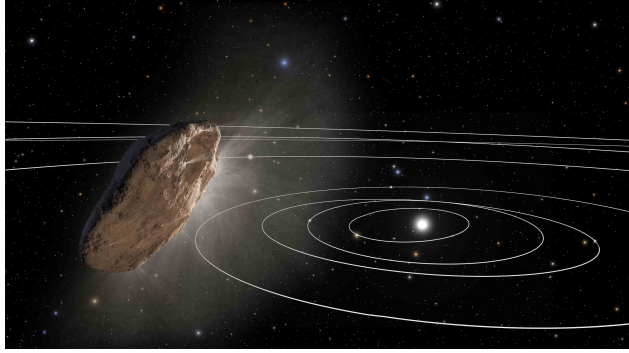


Fig. 1 Artist's illustration 1I/'Oumuamua (credit: NASA, ESA, and STScI).

GNC	=	guidance, navigation, and control
G&C	=	guidance and control
ISO	=	interstellar object
LPC	=	long period comet
LVLH	=	local-vertical local-horizontal frame
MPC	=	model predictive control
SGD	=	stochastic gradient descent
SN-DNN	=	spectrally-normalized deep neural network
S/C	=	spacecraft
TCM	=	trajectory correction maneuver

I. Introduction

INTERSTELLAR objects (ISOs) represent one of the last unexplored classes of solar system objects. They are active or inert objects passing through our solar system on an unbound hyperbolic trajectory about the Sun, which could sample planetesimals and primitive materials that provide vectors to compare our solar system with neighboring exoplanetary star systems [1]. To date, two such objects have been identified and observed: 1I/'Oumuamua [2] discovered in 2017 (Fig. 1); and 2I/Borisov [3] discovered in 2019 (Fig. 2). In 2022, the United States Department of Defense confirmed that a third ISO impacted Earth in 2014, three years before the identification of 'Oumuamua. ISOs are physical laboratories that can enable the study of exosolar systems in-situ rather than remotely using telescopes such as the Hubble or James Webb Space Telescopes.

While remote observation can aid in constraining the level of activity, shape, and spectral signature of ISOs, limiting scientists to Earth-based telescopic observation prevents some of the most impactful science that can be performed. Using a dedicated spacecraft to flyby an ISO opens the doors to high-resolution imaging, mass or dust spectroscopy, and a larger number of vantage points than Earth observation. It could also resolve the target's nucleus shape and spin,



Fig. 2 2I/Borisov near and at perihelion (credit: NASA, ESA, and D. Jewitt (UCLA)).

characterize the volatiles being shed from an active body, reveal fresh surface material using an impactor, and more [4].

The discovery and exploration of ISOs are “once in a lifetime” or maybe “once in a civilization” opportunities, and their exploration is challenging for three main reasons: 1) they are often not discovered until they are close to Earth, meaning that launches to encounter them often require high launch energy; 2) their orbital properties are poorly constrained at launch, generally leading to significant on-board resources to encounter; and 3) the encounter speeds are typically high (> 10 of km/s) requiring fast response autonomous operations. This paper presents an offline deep learning-based robust nonlinear guidance and control (G&C) approach, called Neural-Rendezvous, to autonomously encounter them even in the presence of such large state uncertainty and high-velocity challenges. As outlined in Fig. 3, the guidance, navigation, and control (GNC) of spacecraft for the ISO encounter are split into two segments: 1) the cruise phase, where the spacecraft utilizes state estimation obtained by ground-based telescopes and navigates via ground-in-the-loop operations, and; 2) the terminal phase, where it switches to fully autonomous operation with existing onboard navigation frameworks. The current state of practice and performance of autonomous navigation systems for small bodies like ISOs are discussed in [5, 6]. Neural-Rendezvous is for performing the second phase of the autonomous terminal G&C with the on-board state estimates and is built upon the spectrally-normalized deep neural network (SN-DNN), a neural network that has been successfully used for providing stability guarantees of learning-based feedback controllers [7–9]. It is constructed by the combination of the following new deep learning-based approaches.

We first propose a dynamical system-based SN-DNN for designing a real-time guidance policy that approximates model predictive control (MPC), which is known to be near-optimal in terms of dynamic regret, i.e., the MPC performance minus the optimal performance in hindsight [10–12]. This is to avoid solving MPC optimization at each time instant and compute a spacecraft’s control input autonomously even with its limited online computational capacity. Consistent with our objective of encountering ISOs, it is an SN-DNN [13] with a novel loss function for directly imitating the MPC state trajectory performing dynamics integration, as well as indirectly imitating the MPC control input as in existing methods [14]. We then introduce learning-based min-norm feedback control to be used on top of this guidance policy, which provides an optimal and robust control input, expressed in an analytical form, that minimizes its instantaneous deviation from that of the SN-DNN guidance policy under the incremental stability condition as in the

one of contraction theory [15, 16].

In particular, we rigorously show that: 1) the SN-DNN guidance policy possesses a verifiable optimality gap with respect to the computationally expensive MPC policy; and that 2) when it is equipped with the learning-based min-norm control, the state tracking error bound with respect to the desired state trajectory decreases exponentially in expectation with a finite probability, robustly against the state uncertainty. The latter indicates that the terminal spacecraft deliver error at the ISO encounter, i.e., the shaded blue region in Fig. 3, is probabilistically bounded in expectation, where its size can be modified accordingly to the mission requirement by tuning its feedback control parameters. In numerical simulations with 100 ISO candidates for possible exploration obtained using [17], it is demonstrated that Neural-Rendezvous outperforms other G&C algorithms including (i) the SN-DNN guidance policy; (ii) proportional-derivative (PD) control with a pre-computed desired trajectory; (iii) robust nonlinear tracking control of [18, pp. 397-402] with a precomputed desired trajectory; and (iv) MPC with linearized dynamics [19]. It achieves a delivery error less than 0.2 km under the realistic ISO state uncertainty [6] for 99 % of the ISO candidates, with 8.0×10^{-4} s computational time for its one-step evaluation and control effort less than 0.6 km/s. It is also validated that, when compared with the conventional SN-DNN that imitates the MPC control input, our dynamical system-based SN-DNN indeed reduces the delivery error thanks to the presence of the state trajectory imitation loss. A YouTube video which visualizes these simulation results can be found at https://youtu.be/8h60B_p1fyQ.

Such verifiable and real-time optimality, stability, and robustness guarantees offer indispensable analytical insight on determining whether or not we should utilize Neural-Rendezvous based on the size of the state uncertainty, thereby enhancing conventional black-box machine learning and AI-based G&C approaches with few theoretical guarantees. It is worth noting that our proposed approach and its guarantees are general enough to be used not only for encountering ISOs, but also for solving various nonlinear autonomous rendezvous problems with fast-moving objects, accurately in real-time under external disturbances and various sources of uncertainty resulting from, e.g., state measurement noise, process noise, control execution error, unknown parts of dynamics, or parametric/non-parametric variations of dynamics and environments.

Related Work

The state of practice in realizing asteroid and comet rendezvous missions is to pre-construct an accurate spacecraft state trajectory to the target before launch, and then perform a few trajectory correction maneuvers (TCMs) along the way based on the state measurements obtained by ground-based and onboard navigation schemes [6]. Such a G&C approach is only feasible for targets with sufficient information on their orbital properties in advance, which is not realistic for ISOs visiting our solar system traveling through interstellar space.

The ISO rendezvous problem can be cast as a robust motion planning and control problem that has been investigated in numerous studies in the field of robotics. The most well-developed and commercialized of these G&C methods is

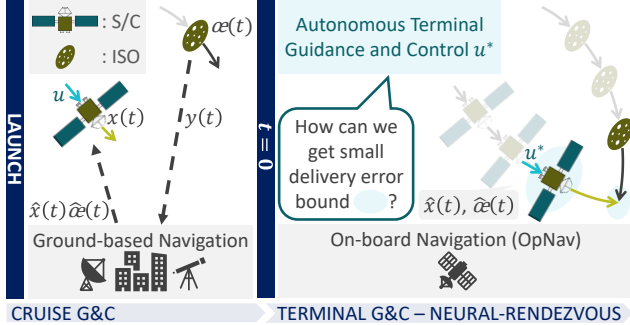


Fig. 3 Illustration of cruise and terminal GNC, where t is time, $\alpha(t)$ is ISO state, $x(t)$ is spacecraft state relative to $\alpha(t)$, $y(t)$ is state measurement of ISO and spacecraft, u is control input, and $\hat{\alpha}(t)$ and $\hat{x}(t)$ are estimated ISO and spacecraft relative state, respectively. Neural-Rendezvous enables obtaining verifiable delivery error bound even under large ISO state uncertainty and high-velocity challenges.

robust MPC [20, 21], which extensively utilizes knowledge about the underlying nonlinear dynamical system to design an optimal control input at each time instant, thereby allowing a spacecraft to use the most updated ISO state information that should get more accurate as it gets closer to the target. When the MPC is augmented with feedback control, robustness against the state uncertainty and various external disturbances can be shown using standard techniques in systems and control theory, such as Lyapunov and contraction theory [16, 22–24]. However, as mentioned earlier, the spacecraft’s onboard computational power is not necessarily sufficient to solve the MPC optimization at each time instant of its TCM, which could lead to failure in accounting for the ISO state that changes dramatically in a few seconds due to the body’s high velocity.

Learning-based control designs have been considered a promising solution to this problem, as they allow replacing these computationally-expensive G&C algorithms with computationally-cheap mathematical models, e.g., neural networks [14, 25–31]. Neural-Rendezvous we present in this paper is a novel variant of a learning-based control design. Its benefits lie in the formal derivation of its optimality gap with respect to the MPC policy as a function of the dynamical system-based SN-DNN learning error, and the robustness and stability guarantee even under the presence of state uncertainty and learning errors, which can be shown by extending the results of [16] for general nonlinear systems to the case of the ISO rendezvous problem.

Notation

We let $\|x\|$ denote the Euclidean norm for a vector $x \in \mathbb{R}^n$, and let $A > 0$, $A \geq 0$, $A < 0$, and $A \leq 0$ denote the symmetric positive definite, positive semi-definite, negative definite, negative semi-definite matrices, respectively, for a square matrix $A \in \mathbb{R}^{n \times n}$. Also, the target celestial bodies will be considered to be ISOs in the subsequent sections for the sake of consistency, but our proposed method should work for long-period comets (LPCs) [32–34], drones, and other fast-moving objects in robotics and aerospace applications, with the same arguments to be presented. In this paper, the new and important results will be stated in Theorems 1–3, and key concepts for understanding our contributions will

be illustrated in Fig. 4–8.

II. Technical Challenges in ISO Exploration

In this paper, we consider the following translational dynamical system of a spacecraft relative to an Interstellar Object (ISO), equipped with feedback control $u \in \mathbb{R}^n \times \mathbb{R}^n \times \mathbb{R}_{\geq 0} \mapsto \mathbb{R}^m$:

$$\dot{x}(t) = f(x(t), \alpha(t), t) + B(x(t), \alpha(t), t)u(\hat{x}(t), \hat{\alpha}(t), t) \quad (1)$$

where $t \in \mathbb{R}_{\geq 0}$ is time, $\alpha \in \mathbb{R}_{\geq 0} \mapsto \mathbb{R}^n$ are the ISO orbital elements evolving by a separate equation of motion (see [35, 36] for details), $x \in \mathbb{R}_{\geq 0} \mapsto \mathbb{R}^n$ is the state of the spacecraft relative to α in a local-vertical local-horizontal (LVLH) frame centered on the ISO [37, pp. 710–712], $f : \mathbb{R}^n \times \mathbb{R}^n \times \mathbb{R}_{\geq 0} \mapsto \mathbb{R}^n$ and $B : \mathbb{R}^n \times \mathbb{R}^n \times \mathbb{R}_{\geq 0} \mapsto \mathbb{R}^{n \times m}$ are known smooth functions [15, 38] (see (2)), and $\hat{\alpha} \in \mathbb{R}_{\geq 0} \mapsto \mathbb{R}^n$ and $\hat{x} \in \mathbb{R}_{\geq 0} \mapsto \mathbb{R}^n$ are the estimated ISO and spacecraft relative state in the LVLH frame given by an on-board navigation scheme, respectively. Particularly when we select x as $x = [p^\top, \dot{p}^\top]^\top$ as its state, where $p \in \mathbb{R}^3$ is the position of the spacecraft relative to the ISO, we have that

$$f(x, \alpha, t) = \begin{bmatrix} \dot{p} \\ -m_{sc}(t)^{-1}(C(\alpha)\dot{p} + G(p, \alpha)) \end{bmatrix}, \quad B(x, \alpha, t) = \begin{bmatrix} \mathbf{0}_{3 \times 3} \\ m_{sc}(t)^{-1}\mathbf{I}_{3 \times 3} \end{bmatrix} \quad (2)$$

where $m_{sc}(t)$ is the mass of the spacecraft described by the Tsiolkovsky rocket equation, and the functions G and C are as given in [15, 36].

Remark 1. *In general, the estimation errors $\|\hat{x}(t) - x(t)\|$ and $\|\hat{\alpha}(t) - \alpha(t)\|$ are expected to decrease with the help of the state-of-the-art onboard navigation schemes as the spacecraft gets closer to the ISO, utilizing more accurate ISO state measurements obtained from an onboard sensor as detailed in [6]. For example, if the extended Kalman filter [39] or contraction theory-based estimator [40–42] is used for navigation, their expected values can be shown to be bounded and exponentially decreasing in t . Although G&C are the focus of our study and thus developing such a navigation technique is beyond our scope, those interested in this field can also refer to, e.g., [5, 6], to tighten the estimation error bound using practical knowledge specific to the ISO dynamics.*

The major design challenges in realizing the ISO encounter, i.e., achieving a sufficiently small spacecraft delivery error with respect to a given desired relative position to flyby or impact the ISO, can be decomposed into the following G&C problems.

(P1) Autonomous terminal guidance responding rapidly to radically changing ISO state

Since the ISO state and its onboard estimate in (1) change dramatically in time due to their poorly constrained orbits with high inclinations and high relative velocities, using a fixed desired trajectory computed at some point earlier in

time could fail to utilize the radically changing ISO state information as much as possible. Therefore, we construct a guidance policy to optimally achieve the smallest spacecraft delivery error for given estimated states $\hat{x}(t)$ and $\hat{\alpha}(t)$ in (1) at time t , and then design a learning-based guidance algorithm that approximates it with a verifiable optimality gap, so the spacecraft can update its desired trajectory autonomously in real-time using the most recent state estimates $\hat{x}(t)$ and $\hat{\alpha}(t)$, which become more accurate as the spacecraft gets closer to the ISO as discussed in Remark 1.

(P2) Feedback tracking control robust against state uncertainty

Although the learning-based terminal guidance in (P1) is useful in exploiting the radically changing state information in real-time, evaluating its robustness property against the ISO and spacecraft relative state uncertainty is difficult in general. We thus design an autonomous nonlinear feedback control algorithm that robustly tracks the desired trajectory with zero spacecraft delivery error computed using (P1), and that guarantees a finite tracking error bound even under the presence of the state uncertainty and the guidance learning error in (P1), while still having a verifiable optimality gap with respect to the optimal guidance policy of (P1).

III. Autonomous Guidance via Dynamical System-Based Deep Learning

This section proposes dynamical system-based deep learning to solve the autonomous terminal guidance problem (P1) in Sec. II. As to be seen in the following, it utilizes the known dynamics of (1) and (2) in approximating a computationally-expensive optimal guidance policy, thereby directly minimizing the deviation of the learned state trajectory from the optimal state trajectory with the smallest spacecraft delivery error at the ISO encounter, possessing a verifiable optimality gap with respect to the optimal guidance policy.

A. Model Predictive Control Problem

Let us first introduce the following definition of an ISO state flow, which maps the ISO state at any given time to the one at time t , so we can account for the rapidly changing ISO state estimate of (1) in our proposed framework.

Definition 1. A flow $\varphi^t(\alpha_0)$, where α_0 is some given ISO state, defines the solution trajectory of the autonomous ISO dynamical system [35, 36] at time t , which satisfies $\varphi^0(\alpha_0) = \alpha_0$ at $t = 0$.

Utilizing the ISO flow given in Definition 1, we consider the following optimal guidance problem for the ISO encounter, given estimated states $\hat{x}(\tau)$ and $\hat{\alpha}(\tau)$ in (1) at $t = \tau$:

$$u^*(\hat{x}(\tau), \hat{\alpha}(\tau), t, \rho) = \arg \min_{u(t) \in \mathcal{U}(t)} \left(c_0 \|p_\xi(t_f) - \rho\|^2 + c_1 \int_{\tau}^{t_f} P(u(t), \xi(t)) dt \right) \quad (3)$$

$$\text{s.t. } \dot{\xi}(t) = f(\xi(t), \varphi^{t-\tau}(\hat{\alpha}(\tau)), t) + B(\xi(t), \varphi^{t-\tau}(\hat{\alpha}(\tau)), t)u(t), \quad t \in (\tau, t_f], \quad \xi(\tau) = \hat{x}(\tau) \quad (4)$$

where $\tau \in [0, t_f]$ is the current time at which the spacecraft solves (3), ξ is the fictitious spacecraft relative state of the

dynamics (4), $\int_{\tau}^{t_f} P(u(t), \xi(t))dt$ is some performance-based cost function, such as L^2 control effort, L^2 trajectory tracking error, and information-based cost [43], $p_{\xi}(t_f)$ is the terminal relative position of the spacecraft satisfying $\xi(t_f) = [p_{\xi}(t_f)^\top, \dot{p}_{\xi}(t_f)^\top]^\top$, ρ is a mission-specific predefined terminal position relative to the ISO at given terminal time t_f ($\rho = 0$ for impacting the ISO), $\mathcal{U}(t)$ is a set containing admissible control inputs, and $c_0 \in \mathbb{R}_{>0}$ and $c_1 \in \mathbb{R}_{\geq 0}$ are the weights on each objective function. This paper assumes that the terminal time t_f is not a decision variable but a fixed constant, as varying it is demonstrated to have a small impact on the objective value of (3) in our simulation setup in Sec. VII. Note that ρ is explicitly considered as one of the inputs to u^* to account for the fact that it could change depending on the target ISO.

Remark 2. *Since it is not realistic to match the spacecraft velocity with that of the ISOs due to their high inclination nature, the terminal velocity tracking error is intentionally not included in the cost function, although it could be with an appropriate choice of P in (3). Also, we can set $c_0 = 0$ and augment the problem with a constraint $\|p_{\xi}(t_f) - \rho\| = 0$ if the problem is feasible with this constraint.*

Since the spacecraft relative state changes dramatically due to the ISO's high relative velocity, as discussed in the problem (P1), and because the actual dynamics are perturbed by the ISO and spacecraft relative state estimation uncertainty, which decreases as t gets closer to t_f (see Remark 1), it is expected that the delivery error at the ISO encounter (i.e., $\|p_{\xi}(t_f) - \rho\|$) becomes smaller as the spacecraft solves (3) more frequently onboard using the updated state estimates in the initial condition (4) as in (1). More specifically, it is desirable to apply the optimal guidance policy solving (3) at each time instant t as follows as in model predictive control (MPC) [19, 44]:

$$u_{\text{mpc}}(\hat{x}(t), \hat{\alpha}(t), t, \rho) = u^*(\hat{x}(t), \hat{\alpha}(t), t, \rho) \quad (5)$$

where u is the control input of (1). Note that τ of u^* in (5) is now changed to t unlike (3), implying we only utilize the solution of (3) at the initial time $t = \tau$. Due to the predictive nature of the MPC, which leverages future predictions of the states $x(t)$ and $\alpha(t)$ for $t \in [\tau, t_f]$ obtained by integrating their dynamics given $\hat{x}(\tau)$ and $\hat{\alpha}(\tau)$ as in (4), the solution of its linearized and discretized version can be shown to be near-optimal [10] in terms of dynamic regret, i.e., the MPC performance minus the optimal performance in hindsight [11]. This would imply that the nonlinear MPC also enjoys similar optimality guarantees when it is solved by the sequential convex programming approach [45–47], which is proven to converge to a point satisfying the KKT conditions [48, pp. 243-244] (see [12]). However, solving the nonlinear optimization problem (3) at each time instant to obtain (5) is not realistic for a spacecraft with limited computational power.

B. Imitation Learning of MPC State and Control Trajectories

In order to compute the MPC of (5) in real-time with a verifiable optimality guarantee, our proposed learning-based terminal guidance policy models it using an SN-DNN [13] defined as follows.

Definition 2. A neural network is the following nonlinear mathematical model to approximately represent training data points $\{(a_i, b_i)\}_{i=1}^{N_d}$ of $b = \psi(a)$, generated by a function ψ , by optimally tuning its hyperparameters W_ℓ , $\ell \in \mathbb{N} \cup [1, N_\ell + 1]$:

$$b_i = \psi_{\text{nn}}(a_i; W_\ell) = T_{N_\ell+1} \circ \phi \circ T_{N_\ell} \circ \cdots \circ \phi \circ T_1(x_i) \quad (6)$$

where $T_\ell(x) = W_\ell x$, \circ denotes composition of functions, and ϕ is an activation function. A neural network with more than two layers (i.e., $N_\ell \geq 2$) is called a deep neural network (DNN). A spectrally-normalized DNN (SN-DNN) is a DNN with its weights W_ℓ normalized as $W_\ell = (C_{\text{nn}} \Omega_\ell) / \|\Omega_\ell\|$, where $C_{\text{nn}} \in \mathbb{R}_{\geq 0}$ is a given constant.

The SN-DNN is known to have the following useful properties [7, 13].

Lemma 1. An SN-DNN is Lipschitz continuous by design with its 2-norm Lipschitz constant $C_{\text{nn}}^{N_\ell+1} L_\phi^{N_\ell}$, where $L_\phi \in \mathbb{R}_{>0}$ is the Lipschitz constant of the activation function ϕ in (6). Also, it is robust to perturbation in its input.

Proof. See Lemma 6.2 of [16]. □

Let us denote the proposed learning-based terminal guidance policy as $u_\ell(\hat{x}(t), \hat{\alpha}(t), t, \rho; \theta_{\text{nn}})$, which models the MPC policy $u_{\text{mpc}}(\hat{x}(t), \hat{\alpha}(t), t, \rho)$ of (5) using the SN-DNN of Definition 2, where $\theta_{\text{nn}} = \{W_\ell\}_{\ell=1}^{N_\ell+1}$ is its hyperparameter given in (6). The following definition of the process induced by the spacecraft dynamics with u_{mpc} and u_ℓ , which map the ISO and spacecraft relative state at any given time to their respective spacecraft relative state at time t , is useful for simplifying notation in our framework.

Definition 3. Mappings denoted as $\varphi_\ell^t(x_\tau, \alpha_\tau, \tau, \rho; \theta_{\text{nn}})$ and $\varphi_{\text{mpc}}^t(x_\tau, \alpha_\tau, \tau, \rho)$ (called processes [49, p. 24]) define the solution trajectories of the following non-autonomous dynamical systems at time t , controlled by the SN-DNN and MPC policy, respectively:

$$\dot{\xi}(t) = f(\xi(t), \varphi^{t-\tau}(\alpha_\tau), t) + B(\xi(t), \varphi^{t-\tau}(\alpha_\tau), t)u_\ell(\xi(t), \varphi^{t-\tau}(\alpha_\tau), t, \rho; \theta_{\text{nn}}), \quad \xi(\tau) = x_\tau \quad (7)$$

$$\dot{\xi}(t) = f(\xi(t), \varphi^{t-\tau}(\alpha_\tau), t) + B(\xi(t), \varphi^{t-\tau}(\alpha_\tau), t)u_{\text{mpc}}(\xi(t), \varphi^{t-\tau}(\alpha_\tau), t, \rho), \quad \xi(\tau) = x_\tau \quad (8)$$

where $\tau \in [0, t_f]$, t_f and ρ are the given terminal time and relative position at the ISO encounter as in (4), α_τ and x_τ are some given ISO and spacecraft relative state at time $t = \tau$, respectively, f and B are given in (1) and (2), and $\varphi^{t-\tau}(\alpha_\tau)$ is the ISO state trajectory with $\varphi^0(\alpha_\tau) = \alpha_\tau$ at $t = \tau$ as given in Definition 1.

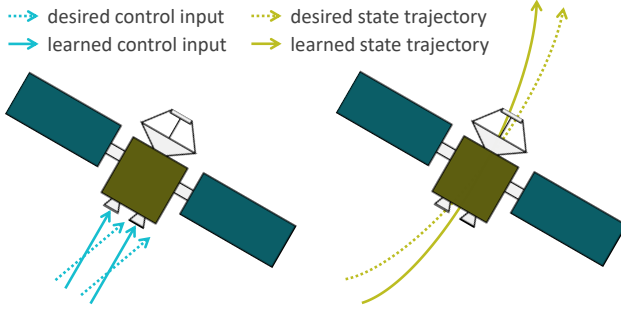


Fig. 4 Left: SN-DNN trained to imitate desired control input (first term of (9)); right: SN-DNN trained to imitate desired state trajectory (second term of (9)).

Let $(\bar{x}, \bar{\alpha}, \bar{t}, \bar{\rho}, \Delta\bar{t})$ denote a sampled data point for the spacecraft state, ISO state, current time, desired terminal relative position, and time of integration to be used in (9), respectively. Also, let $\text{Unif}(\mathcal{S})$ be the uniform distribution over a compact set \mathcal{S} , which produces $(\bar{x}, \bar{\alpha}, \bar{t}, \bar{\rho}, \Delta\bar{t}) \sim \text{Unif}(\mathcal{S})$. Using Definition 3, we introduce the following new loss function to be minimized by optimizing the hyperparameter θ_{nn} of the SN-DNN guidance policy $u_\ell(\hat{x}(t), \hat{\alpha}(t), t, \rho; \theta_{\text{nn}})$:

$$\mathcal{L}_{\text{nn}}(\theta_{\text{nn}}) = \mathbb{E} \left[\|u_\ell(\bar{x}, \bar{\alpha}, \bar{t}, \bar{\rho}; \theta_{\text{nn}}) - u_{\text{mpc}}(\bar{x}, \bar{\alpha}, \bar{t}, \bar{\rho})\|_{C_u}^2 + \|\varphi_\ell^{\bar{t}+\Delta\bar{t}}(\bar{x}, \bar{\alpha}, \bar{t}, \bar{\rho}; \theta_{\text{nn}}) - \varphi_{\text{mpc}}^{\bar{t}+\Delta\bar{t}}(\bar{x}, \bar{\alpha}, \bar{t}, \bar{\rho})\|_{C_x}^2 \right] \quad (9)$$

where $\|(\cdot)\|_{C_x}$ and $\|(\cdot)\|_{C_u}$ are the weighted Euclidean 2-norm given as $\|(\cdot)\|_{C_u}^2 = (\cdot)^\top C_u (\cdot)$ and $\|(\cdot)\|_{C_x}^2 = (\cdot)^\top C_x (\cdot)$ for symmetric positive definite weight matrices $C_u, C_x > 0$, and $\varphi_\ell^t(\bar{x}, \bar{\alpha}, \bar{t}, \bar{\rho}; \theta_{\text{nn}})$ and $\varphi_{\text{mpc}}^t(\bar{x}, \bar{\alpha}, \bar{t}, \bar{\rho})$ are the solution trajectories with the SN-DNN and MPC guidance policy given in Definition 3, respectively.

Existing learning methods [16, 28] indirectly imitate a given desired state trajectory by imitating the desired control policy using only the first term of (9). As can be seen from the loss function (9) and as illustrated in Fig. 4, a key distinction of our proposed learning-based guidance from existing work is that we directly train the SN-DNN to also minimize the deviation of the state trajectory with the SN-DNN guidance policy from the desired MPC state trajectory itself using the second term of (9). This is to properly account for the fact that the learning objective is not only to minimize $\|u_\ell - u_{\text{mpc}}\|$, but to imitate the optimal trajectory with the smallest spacecraft delivery error at the ISO encounter as discussed in the problem (P1). We will see how the selection of the weight matrices C_u and C_x affects the control performance of u_ℓ in Sec. VII.

Remark 3. As in standard learning algorithms for neural networks including stochastic gradient descent (SGD) [50, 51], the expectation of the loss function (9) can be approximated using sampled data points as follows:

$$\mathcal{L}_{\text{emp}}(\theta_{\text{nn}}) = \sum_{i=1}^{N_d} \|u_\ell(\bar{x}_i, \bar{\alpha}_i, \bar{t}_i, \bar{\rho}_i; \theta_{\text{nn}}) - u_{\text{mpc}}(\bar{x}_i, \bar{\alpha}_i, \bar{t}_i, \bar{\rho}_i)\|_{C_u}^2 + \|\varphi_\ell^{\bar{t}_i+\Delta\bar{t}_i}(\bar{x}_i, \bar{\alpha}_i, \bar{t}_i, \bar{\rho}_i; \theta_{\text{nn}}) - \varphi_{\text{mpc}}^{\bar{t}_i+\Delta\bar{t}_i}(\bar{x}_i, \bar{\alpha}_i, \bar{t}_i, \bar{\rho}_i)\|_{C_x}^2 \quad (10)$$

Table 1 Notations in Theorem 1.

L_ℓ	2-norm Lipschitz constant of u_ℓ in $\mathbb{R}_{>0}$, guaranteed to exist due to Lemma 1
N_d	Number of training data points
$\mathcal{S}_{\text{test}}$	Any compact test set containing (x, α, t, ρ) , not necessarily training set $\mathcal{S}_{\text{train}}$ itself
u_ℓ	Learning-based terminal guidance policy that models u_{mpc} by SN-DNN using loss function given in (9)
u_{mpc}	Optimal MPC terminal guidance policy given in (5)
(x, α, t, ρ)	Test data point for S/C relative state, ISO state, current time, and desired terminal relative position of (4), respectively
$(\bar{x}_i, \bar{\alpha}_i, \bar{t}_i, \bar{\rho}_i)$	Training data point for S/C relative state, ISO state, current time, and desired terminal relative position of (4), respectively, where $i \in \mathbb{N} \cup [1, N_d]$
Π_{train}	Training dataset containing finite number of training data points, i.e., $\Pi_{\text{train}} = \{(\bar{x}_i, \bar{\alpha}_i, \bar{t}_i, \bar{\rho}_i)\}_{i=1}^{N_d}$

where the training data points $\{(\bar{x}_i, \bar{\alpha}_i, \bar{t}_i, \bar{\rho}_i)\}_{i=1}^{N_d}$ are drawn independently from $\text{Unif}(\mathcal{S})$.

C. Optimality Gap of Deep Learning-Based Guidance

Since an SN-DNN Definition 2 is Lipschitz bounded by design and robust to perturbation as in Lemma 1, the optimality gap of the guidance framework u_ℓ introduced in Sec. III.B can be bounded as in the following theorem, where the notations are summarized in Table 1 and the proof concept is illustrated in Fig. 5.

Theorem 1. Suppose that u_{mpc} is Lipschitz with its 2-norm Lipschitz constant $L_{\text{mpc}} \in \mathbb{R}_{>0}$. If u_ℓ is trained using the empirical loss function (10) of Remark 3 to have $\exists \epsilon_{\text{train}} \in \mathbb{R}_{\geq 0}$ s.t.

$$\sup_{i \in \mathbb{N} \cup [1, N_d]} \|u_\ell(\bar{x}_i, \bar{\alpha}_i, \bar{t}_i, \bar{\rho}_i; \theta_{\text{nn}}) - u_{\text{mpc}}(\bar{x}_i, \bar{\alpha}_i, \bar{t}_i, \bar{\rho}_i)\| \leq \epsilon_{\text{train}} \quad (11)$$

then we have the following bound:

$$\|u_\ell(x, \alpha, t, \rho; \theta_{\text{nn}}) - u_{\text{mpc}}(x, \alpha, t, \rho)\| \leq \epsilon_{\text{train}} + r(x, \alpha, t, \rho)(L_\ell + L_{\text{mpc}}) = \epsilon_{\ell u}, \quad \forall (x, \alpha, t, \rho) \in \mathcal{S}_{\text{test}} \quad (12)$$

where $r(x, \alpha, t, \rho) = \inf_{i \in \mathbb{N} \cup [1, N_d]} \sqrt{\|\bar{x}_i - x\|^2 + \|\bar{\alpha}_i - \alpha\|^2 + (\bar{t}_i - t)^2 + \|\bar{\rho}_i - \rho\|^2}$.

Proof. Let $\eta = (x, \alpha, t, \rho)$ be a test element in $\mathcal{S}_{\text{test}}$ (i.e., $\eta \in \mathcal{S}_{\text{test}}$) and let $\bar{\zeta}_j(\eta)$ be the training data point in Π_{train} (i.e., $\bar{\zeta}_j(\eta) \in \Pi_{\text{train}}$) that achieves the infimum of $r(\eta)$ with $i = j$ for a given $\eta \in \mathcal{S}_{\text{test}}$. Since u_ℓ and u_{mpc} are Lipschitz by design and by assumption, respectively, we have for any $\eta \in \mathcal{S}_{\text{test}}$ that

$$\begin{aligned} \|u_\ell(\eta; \theta_{\text{nn}}) - u_{\text{mpc}}(\eta)\| &\leq \|u_\ell(\bar{\zeta}_j(\eta); \theta_{\text{nn}}) - u_{\text{mpc}}(\bar{\zeta}_j(\eta))\| + \|u_\ell(\eta; \theta_{\text{nn}}) - u_\ell(\bar{\zeta}_j(\eta); \theta_{\text{nn}})\| + \|u_{\text{mpc}}(\eta) - u_{\text{mpc}}(\bar{\zeta}_j(\eta))\| \\ &\leq \|u_\ell(\bar{\zeta}_j(\eta); \theta_{\text{nn}}) - u_{\text{mpc}}(\bar{\zeta}_j(\eta))\| + r(\eta)(L_\ell + L_{\text{mpc}}) \leq \epsilon_{\text{train}} + r(\eta)(L_\ell + L_{\text{mpc}}) \end{aligned}$$

where the second inequality follows from the definition of $\bar{\zeta}_j(\eta)$ and the third inequality follows from (11) and the fact

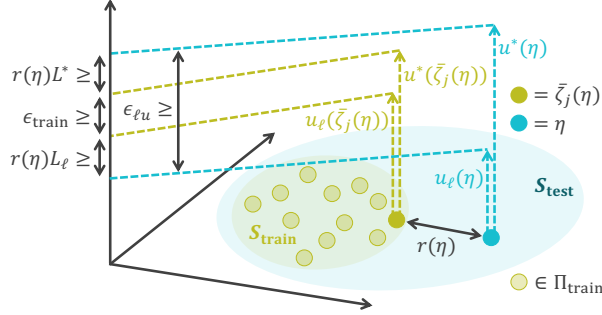


Fig. 5 Illustration of optimality gap (12) in Theorem 1, where S_{train} denotes training set in which training data $(\bar{x}_i, \bar{\alpha}_i, \bar{t}_i, \bar{\rho}_i) \in \Pi_{\text{train}}$ is sampled.

that $\bar{z}_j(\eta) \in \Pi_{\text{train}}$. This relation leads to the desired result (12) as it holds for any $\eta \in S_{\text{test}}$. \square

The major strength of the SN-DNN is that it provides a verifiable optimality gap even for data points not in its training set, using spectral normalization for Lipschitz regularization, which indicates that it still benefits from the near-optimal guarantee of the MPC in terms of dynamic regret [10–12] as discussed below (5). As illustrated in Fig. 5 for clarifying the proof of Theorem 1, each term in the optimality gap (12) can be interpreted as follows:

- 1) ϵ_{train} of (11) is the training error of the SN-DNN, expected to decrease as the learning proceeds using SGD.
- 2) $r(\eta)$ is the closest distance from the test element $\eta \in S_{\text{test}}$ to a training data point in Π_{train} , expected to decrease as the number of data points N_d in Π_{train} increases and as the training set S_{train} gets larger.
- 3) The Lipschitz constant L_ℓ is a design parameter we could arbitrarily choose when constructing the SN-DNN.
- 4) We could also treat L_{mpc} as a design parameter by adding a Lipschitz constraint, $\|\partial u_{\text{mpc}} / \partial \eta\| \leq L_{\text{mpc}}$, in solving (3).

Note that ϵ_{train} and $r(\eta)$ can always be computed numerically for a given η as the dataset Π_{train} only has a finite number of data points. Furthermore, since the proposed guidance framework trains the SN-DNN to also imitate the desired state trajectory using the second term of (9), we could achieve a bound similar to (12) of Theorem 1 even for the optimality gap of the learned state trajectory with the SN-DNN guidance policy, assuming the whole network as in (7), which outputs integrated states given initial states, is Lipschitz. The pseudo-code for constructing the proposed dynamical system-based SN-DNN for autonomous guidance is given in Algorithm 1, where we utilize SGD and back-propagation techniques in standard neural network training on top of the dynamics integration given in (7) and (8).

Remark 4. *Obtaining a tighter and more general optimality gap of the learned control and state trajectories has been an active field of research [52–55]. Particularly for a neural network equipped with a dynamical structure as in our proposed approach, we could refer to generalization bounds for the neural ordinary differential equations [56–61], or use systems and control theoretical methods to augment it with stability and robustness properties [62, 63]. We could also consider combining the SN-DNN with neural networks that have enhanced structural guarantees of robustness,*

including robust implicit networks [64, 65] and robust equilibrium networks [66, 67].

Algorithm 1: Dynamical System-Based SN-DNN Guidance

Inputs :Training set $\mathcal{S}_{\text{train}}$ and test set $\mathcal{S}_{\text{test}}$
Outputs :Trained dynamical system-based SN-DNN

A. Training Data Sampling

for $i \leftarrow 1$ **to** N_d **do**

 Sample $\bar{\zeta}_i = (\bar{x}_i, \bar{\alpha}_i, \bar{t}_i, \bar{\rho}_i, \Delta\bar{t}_i) \sim \text{Unif}(\mathcal{S}_{\text{train}})$
 Sample $\bar{\eta}_i = (\bar{x}_i, \bar{\alpha}_i, \bar{t}_i, \bar{\rho}_i, \Delta\bar{t}_i) \sim \text{Unif}(\mathcal{S}_{\text{test}})$
 Evaluate $u_{\text{mpc}}(\bar{x}_i, \bar{\alpha}_i, \bar{t}_i, \bar{\rho}_i)$ of (5) for $\bar{\zeta}_i$ and $\bar{\eta}_i$
 Integrate (8) with $\bar{\zeta}_i$ and $\bar{\eta}_i$ to get $\varphi_{\text{mpc}}^{\bar{t}_i + \Delta\bar{t}_i}(\bar{x}_i, \bar{\alpha}_i, \bar{t}_i, \bar{\rho}_i)$

Save training and test data as $\mathcal{D}_{\text{train}}$ and $\mathcal{D}_{\text{test}}$

B. Dynamical System-Based SN-DNN Training

for $\text{epoch} \leftarrow 1$ **to** *number of epochs* **do**

for *training batch* $\in \mathcal{D}_{\text{train}}$ **do**

 Evaluate $u_{\ell}(\bar{x}_i, \bar{\alpha}_i, \bar{t}_i, \bar{\rho}_i; \theta_{\text{nn}})$ for *training batch*
 Integrate (7) for *training batch* to get $\varphi_{\ell}^{\bar{t}_i + \Delta\bar{t}_i}(\bar{x}_i, \bar{\alpha}_i, \bar{t}_i, \bar{\rho}_i; \theta_{\text{nn}})$
 Train SN-DNN with loss (10) using SGD

 Compute *test loss* with (10) for $\mathcal{D}_{\text{test}}$

 Compute *error bounds* (12) of Theorem 1 and Remark 4 for $\mathcal{D}_{\text{test}}$

if *test loss & error bounds are small enough* **then**

break

Although the optimality gap discussed in Theorem 1 and in Remark 4 are useful in that they provide mathematical guarantees for learning-based frameworks only with the Lipschitz assumption (e.g., it could prove safety in the learning-based MPC framework [14]). However, when the system is perturbed by the state uncertainty as in (1), we could only guarantee that the distance between the state trajectories controlled by u_{mpc} of (5) and u_{ℓ} of Theorem 1 is bounded by a function that increases exponentially with time [16, 28]. In Sec. IV and V, we will see how such a conservative bound can be replaced by a decreasing counterpart.

IV. Deep learning-Based Optimal Tracking Control

This section proposes a feedback control policy to be used on top of the SN-DNN terminal guidance policy u_{ℓ} of Theorem 1 in Sec. III. In particular, we utilize u_{ℓ} to design the desired trajectory with zero spacecraft delivery error and then construct pointwise optimization-based tracking control with a Lyapunov stability condition, which can be shown to have an analytical solution for real-time implementation. In Sec. V, we will see that this framework plays an essential part in solving the control problem (P2) of Sec. II.

Remark 5. For notational convenience, we drop the dependence on the desired terminal relative position ρ of (4) in u_{ℓ} , u_{mpc} , φ_{ℓ}^t , and φ_{mpc}^t in the subsequent sections, as it is time-independent and thus does not affect the arguments to be made in the following. Note that the SN-DNN is still to be trained regarding ρ as one of its inputs as outlined in Algorithm 2, so we do not have to retrain SN-DNNs every time we change ρ .

Table 2 Summary of ISO state flow and spacecraft state processes in Definitions 1 and 3, where u_ℓ and u_{mpc} are SN-DNN and MPC guidance policies, respectively. Note that the dependence on the terminal position ρ is omitted as explained in Remark 5.

$\varphi^{t-\tau}(\alpha_\tau)$	Solution trajectory of ISO dynamics at time t which satisfies $\varphi^0(\alpha_\tau) = \alpha_\tau$
$\varphi_\ell^t(x_\tau, \alpha_\tau, \tau; \theta_{\text{nn}})$	Solution trajectory of S/C relative dynamics at time t , controlled by u_ℓ with no state estimation error, which satisfies $\varphi_\ell^\tau(x_\tau, \alpha_\tau, \tau; \theta_{\text{nn}}) = x_\tau$ at $t = \tau$ and $\alpha(t) = \varphi^{t-\tau}(\alpha_\tau)$
$\varphi_{\text{mpc}}^t(x_\tau, \alpha_\tau, \tau)$	Solution trajectory of S/C relative dynamics at time t , controlled by u_{mpc} with no state estimation error, which satisfies $\varphi_{\text{mpc}}^\tau(x_\tau, \alpha_\tau, \tau) = x_\tau$ at $t = \tau$ and $\alpha(t) = \varphi^{t-\tau}(\alpha_\tau)$

A. Desired State Trajectory with Zero Delivery Error

Let us recall the definitions of the ISO state flow and spacecraft state processes of Definitions 1 and 3 summarized in Table 2. Ideally at some given time $t = t_d \in [0, t_f]$ when the spacecraft possesses enough information on the ISO, we would like to construct a desired trajectory using the estimated states $\hat{\alpha}(t_d)$ and $\hat{x}(t_d)$ s.t. it ensures zero spacecraft delivery error at the ISO encounter assuming zero state estimation errors for $t \in [t_d, t_f]$ in (1). This can be achieved by obtaining a desired state trajectory as $\varphi_\ell^t(x_f, \alpha_f, t_f)$ of Table 2 with $\alpha_f = \varphi^{t_f-t_d}(\hat{\alpha}(t_d))$, i.e., by solving the following dynamics with the SN-DNN terminal guidance policy u_ℓ (7) backward in time:

$$\dot{\xi}(t) = f(\xi(t), \varphi^{t-t_d}(\hat{\alpha}(t_d)), t) + B(\xi(t), \varphi^{t-t_d}(\hat{\alpha}(t_d)), t)u_\ell(\xi(t), \varphi^{t-t_d}(\hat{\alpha}(t_d)), t; \theta_{\text{nn}}), \quad \xi(t_f) = x_f \quad (13)$$

where the property of the ISO solution flow in Table 2 introduced in Definition 1, $\varphi^{t-t_f}(\alpha_f) = \varphi^{t-t_f}(\varphi^{t_f-t_d}(\alpha(t_d))) = \varphi^{t-t_d}(\alpha(t_d))$, is used to get (13), t_f is the given terminal time at the ISO encounter as in (4), and the ideal spacecraft terminal relative state x_f is defined as

$$x_f = \begin{bmatrix} \rho \\ C_{\text{s2v}} \varphi_\ell^{t_f}(\hat{x}(t_d), \hat{\alpha}(t_d), t_d) \end{bmatrix} \quad (14)$$

where ρ is the desired terminal relative position given in (4), $\varphi_\ell^{t_f}(\hat{x}(t_d), \hat{\alpha}(t_d), t_d)$ is the spacecraft relative state at $t = t_f$ obtained by integrating the dynamics forward as in Table 2, and $C_{\text{s2v}} = [\mathbf{O}_{3 \times 3} \ \mathbf{I}_{3 \times 3}] \in \mathbb{R}^{3 \times 6}$ is a matrix that maps the spacecraft relative state to its velocity vector. Figure 6 illustrates the construction of such a desired trajectory.

Remark 6. *Although the desired state trajectory design depicted in Fig. 6 involves backward and forward integration (13) and (14) as in Definition 3, the SN-DNN approximation of the MPC policy allows performing it within a short period. In fact, when measured using the Mid 2015 MacBook Pro laptop, it takes only about 3.0×10^{-4} s for numerically integrating the dynamics for one step using the fourth-order Runge–Kutta method (e.g., it takes ~ 3 s to get the desired trajectory for $t_d = 0$ (s) and $t_f = 10000$ (s) with the discretization time step 1 s). The computational time should decrease as t_d becomes larger. Section V.C delineates how we utilize such a desired trajectory in real-time with the feedback control to be introduced in Sec. IV.B.*

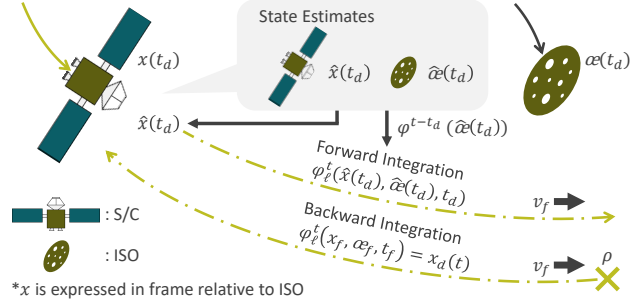


Fig. 6 Illustration of desired trajectory discussed in Sec. IV.A, where $v_f = C_{s2v}\varphi_\ell^{tf}(\hat{x}(t_d), \hat{\alpha}(t_d), t_d)$ as in (14). Spacecraft obtains desired trajectory x_d of (15) as a result of backward integration (see Remark 6).

B. Deep Learning-Based Pointwise Min-Norm Control

Using the results given in Sec. IV.A, we present one approach to designing pointwise optimal tracking control resulting in verifiable spacecraft delivery error, even under the presence of state uncertainty. For notational simplicity, let us denote the desired spacecraft relative state and ISO state trajectories of (13), constructed using $\hat{x}(t_d)$ and $\hat{\alpha}(t_d)$ at $t = t_d$ with the terminal state (14) as illustrated in Fig. 6, as follows:

$$x_d(t) = \varphi_\ell^t(x_f, \alpha_f, t_f), \quad \alpha_d(t) = \varphi^{t-t_d}(\hat{\alpha}(t_d)). \quad (15)$$

Also, assuming that we select x as $x = [p^\top, \dot{p}^\top]^\top$ as the state of (1) as in (2), where $p \in \mathbb{R}^3$ is the position of the spacecraft relative to the ISO, let $\mathcal{J}(x, \alpha, t)$ and $\mathcal{B}(x, \alpha, t)$ be defined as follows:

$$\mathcal{J}(x, \alpha, t) = C_{s2v}f(x, \alpha, t), \quad \mathcal{B}(x, \alpha, t) = C_{s2v}B(x, \alpha, t), \quad (16)$$

where f and B are given in (1) and $C_{s2v} = [O_{3 \times 3} \ I_{3 \times 3}] \in \mathbb{R}^{3 \times 6}$ as in (14). Note that the relations (16) imply

$$\ddot{p} = \mathcal{J}(x, \alpha, t) + \mathcal{B}(x, \alpha, t)u(\hat{x}, \hat{\alpha}, t) \quad (17)$$

Given the desired trajectory (15), $x_d = [p_d^\top, \dot{p}_d^\top]^\top$, which achieves zero spacecraft delivery error at the ISO encounter when the state estimation errors are zero for $t \in [t_d, t_f]$ in (1), we propose to design a controller u of (1) and (17) as follows:

$$u_\ell^*(\hat{x}, \hat{\alpha}, t; \theta_{nn}) = u_\ell(x_d(t), \alpha_d(t), t; \theta_{nn}) + k(\hat{x}, \hat{\alpha}, t) \quad (18)$$

$$k(\hat{x}, \hat{\alpha}, t) = \begin{cases} 0 & \text{if } \Upsilon(\hat{x}, \hat{\alpha}, t) \leq 0 \\ -\frac{\Upsilon(\hat{x}, \hat{\alpha}, t)(\dot{p} - \varphi_d(\hat{p}, t))}{\|\dot{p} - \varphi_d(\hat{p}, t)\|^2} & \text{otherwise} \end{cases} \quad (19)$$

with Υ and ϱ_d defined as

$$\begin{aligned}\Upsilon(\hat{x}, \hat{\alpha}, t) &= (\dot{\hat{p}} - \varrho_d(\hat{p}, t))^T M(t) (\mathcal{J}(\hat{x}, \hat{\alpha}, t) - \mathcal{J}(x_d(t), \alpha_d(t), t) + \Lambda(\dot{\hat{p}} - \dot{p}_d(t)) + \alpha(\dot{\hat{p}} - \varrho_d(\hat{p}, t))) \\ \varrho_d(\hat{p}, t) &= -\Lambda(\hat{p} - p_d(t)) + \dot{p}_d(t)\end{aligned}\quad (20)$$

where $\hat{p} \in \mathbb{R}^3$ is the estimated position of the spacecraft relative to the ISO s.t. $\hat{x} = [\hat{p}^T, \dot{\hat{p}}^T]^T$, u_ℓ is the SN-DNN terminal guidance policy of Theorem 1, α_d , \mathcal{J} , and \mathcal{B} are given in (15) and (16), $\Lambda > 0$ is a given symmetric positive definite matrix, $\alpha \in \mathbb{R}_{>0}$ is a given positive constant, and $M(t) = m_{\text{sc}}(t)I_{3 \times 3}$ for the spacecraft mass $m_{\text{sc}}(t)$ given in (2). This control policy can be shown to possess the following pointwise optimality property, in addition to the robustness and stability guarantees to be seen in Sec. V.

Consider the following optimization problem, which computes an optimal control input that minimizes its instantaneous deviation from that of the SN-DNN guidance policy at each time instant, under an incremental Lyapunov stability condition:

$$u_\ell^*(\hat{x}, \hat{\alpha}, t; \theta_{\text{nn}}) = \arg \min_{u \in \mathbb{R}^m} \|u - u_\ell(x_d(t), \alpha_d(t), t; \theta_{\text{nn}})\|^2 \quad (21)$$

$$\begin{aligned}\text{s.t. } & \frac{\partial V}{\partial \dot{\hat{p}}}(\dot{\hat{p}}, \varrho_d(\hat{p}, t), t)(\mathcal{J}(\hat{x}, \hat{\alpha}, t) + \mathcal{B}(\hat{x}, \hat{\alpha}, t)u) \\ & + \frac{\partial V}{\partial \varrho_d}(\dot{\hat{p}}, \varrho_d(\hat{p}, t), t)(\ddot{p}_d(t) - \Lambda(\dot{\hat{p}} - \dot{p}_d(t))) \leq -2\alpha V(\dot{\hat{p}}, \varrho_d(\hat{p}, t), t)\end{aligned}\quad (22)$$

where V is a non-negative function defined as

$$V(\dot{\hat{p}}, \varrho_d, t) = (\dot{\hat{p}} - \varrho_d)^T M(t) (\dot{\hat{p}} - \varrho_d) \quad (23)$$

and the other notation is as given in (18).

Lemma 2. *The optimization problem (21) is always feasible, and the controller (18) defines its analytical optimal solution for the spacecraft relative dynamical system (2). Furthermore, substituting $u = u_\ell(x_d(t), \alpha_d(t), t; \theta_{\text{nn}})$ into (22) yields $\Upsilon(\hat{x}, \hat{\alpha}, t) \leq 0$, which implies the controller (18) modulates the desired input, $u_\ell(x_d(t), \alpha_d(t), t; \theta_{\text{nn}})$, only when necessary to ensure the stability condition (22).*

Proof. See Appendix. □

Let us emphasize again that, as proven in Lemma 2, the deviation term $k(\hat{x}, \hat{\alpha}, t)$ of the controller (18) is non-zero only when the stability condition (22) cannot be satisfied with the SN-DNN terminal guidance policy u_ℓ of Theorem 1. This result can be viewed as an extension of the control methodology of [68, 69], where the Lagrangian system-type structure of the spacecraft relative dynamics is used extensively to obtain the analytical solution (18) of the quadratic

Table 3 Notations in Sec. IV.C.

$C_{\text{iso}}(r), C_{\text{sc}}(r)$	Tubes of radius $r \in \mathbb{R}_{>0}$ centered around desired trajectories x_d and α_d given in (15), i.e., $C_{\text{iso}}(r) = \bigcup_{t \in [t_s, t_f]} \{\xi \in \mathbb{R}^n \mid \ \xi - \alpha_d(t)\ < r\} \subset \mathbb{R}^n$ and $C_{\text{sc}}(r) = \bigcup_{t \in [t_s, t_f]} \{\xi \in \mathbb{R}^n \mid \ \xi - x_d(t)\ < r\} \subset \mathbb{R}^n$
$\mathcal{E}_{\text{iso}}, \mathcal{E}_{\text{sc}}$	Subsets of \mathbb{R}^n that have ISO and S/C state estimation error vectors $\ \hat{\alpha}(t) - \alpha(t)\ $ and $\ \hat{x}(t) - x(t)\ $, respectively, where given on-board navigation scheme is valid (e.g., region of attraction [70, pp. 312-322])
$\mathbb{E}_{Z_1} [\cdot]$	Conditional expected value operator s.t. $\mathbb{E} [\cdot \mid x(t_1) = x_1, \hat{x}(t_1) = \hat{x}_1, \alpha(t_1) = \alpha_1, \hat{\alpha}(t_1) = \hat{\alpha}_1]$
t_f	Given terminal time at ISO encounter as in (4)
t_s	Time when S/C activates SN-DNN min-norm control policy (18) of Lemma 2
Z_1	Tuple of true and estimated ISO and S/C state at time $t = t_1$, i.e., $Z_1 = (\alpha_1, \hat{\alpha}_1, x_1, \hat{x}_1)$
$\varsigma^t(Z_1, t_1)$	Expected estimation error upper bound at time $t = t_1$ given Z_1 at time $t = t_1$, which can be determined based on choice of navigation techniques (see Remark 1)

optimization problem (21), for the sake of its real-time implementation.

C. Assumptions for Robustness and Stability

Before proceeding to the next section on proving the robustness and stability properties of the SN-DNN min-norm control of (18) of Lemma 2, let us make a few assumptions with the notations given in Table 3, the first of which is that the spacecraft has access to an on-board navigation scheme that satisfies the following conditions.

Assumption 1. *Let the probability of the error vectors remaining in \mathcal{E}_{iso} and \mathcal{E}_{sc} be bounded as follows for $\exists \varepsilon_{\text{est}} \in \mathbb{R}_{\geq 0}$:*

$$\mathbb{P} \left[\bigcap_{t \in [0, t_f]} (\hat{\alpha}(t) - \alpha(t)) \in \mathcal{E}_{\text{iso}} \cap (\hat{x}(t) - x(t)) \in \mathcal{E}_{\text{sc}} \right] \geq 1 - \varepsilon_{\text{est}}. \quad (24)$$

We assume that if the event of (24) has occurred, then we have the following bound for any $t_1, t_2 \in [0, t_f]$ s.t. $t_1 \leq t_2$:

$$\mathbb{E}_{Z_1} \left[\sqrt{\|\hat{\alpha}(t) - \alpha(t)\|^2 + \|\hat{x}(t) - x(t)\|^2} \right] \leq \varsigma^t(Z_1, t_1), \quad \forall t \in [t_1, t_2]. \quad (25)$$

We also assume that given the 2-norm estimation error satisfies $\sqrt{\|\hat{\alpha}(t) - \alpha(t)\|^2 + \|\hat{x}(t) - x(t)\|^2} < c_e$ for $c_e \in \mathbb{R}_{\geq 0}$ at time $t = t_s$, then it satisfies this bound for $\forall t \in [t_s, t_f]$ with probability at least $1 - \varepsilon_{\text{err}}$, where $\exists \varepsilon_{\text{err}} \in \mathbb{R}_{\geq 0}$.

If the extended Kalman filter [39] or contraction theory-based estimator [40–42] is used for navigation with disturbances expressed as the Gaussian white noise processes, then we have $\varsigma^t(Z_1, t_1) = e^{-\beta(t-t_1)} \sqrt{\|\hat{\alpha}_1 - \alpha_1\|^2 + \|\hat{x}_1 - x_1\|^2} + c$, where $Z_1 = (\alpha_1, \hat{\alpha}_1, x_1, \hat{x}_1)$ and β and c are some given positive constants (see Example 1). The last statement of the boundedness of the estimation error is expected for navigation schemes resulting in a decreasing estimation error, and can be shown formally using Ville’s maximal inequality for supermartingales [71, pp. 79-83] with an appropriate Lyapunov-like function for navigation synthesis [71, pp. 79-83] (see Lemma 3 in Appendix for similar computation in control synthesis). Note that if $\mathcal{E}_{\text{iso}} = \mathcal{E}_{\text{sc}} = \mathbb{R}^n$, i.e., the bound (25) holds globally, then we have $\varepsilon_{\text{est}} = 0$. Let us further

make the following assumption on the SN-DNN min-norm control policy (18).

Assumption 2. *We assume that k of (19) is locally Lipschitz in its first two arguments, i.e., $\exists r_{\text{sc}}, r_{\text{iso}}, L_k \in \mathbb{R}_{>0}$ s.t.*

$$\|k(x_1, \alpha_1, t) - k(x_2, \alpha_2, t)\| \leq L_k \sqrt{\|\alpha_1 - \alpha_2\|^2 + \|x_1 - x_2\|^2}, \quad \forall \alpha_1, \alpha_2 \in C_{\text{iso}}(r_{\text{iso}}), \quad x_1, x_2 \in C_{\text{sc}}(r_{\text{sc}}), \quad t \in [t_s, t_f]. \quad (26)$$

We also assume that r_{iso} and r_{sc} are large enough to have $r_{\text{iso}} - 2c_e \geq 0$ and $r_{\text{sc}} - 2c_e \geq 0$ for c_e of Assumption 1, and that the set $C_{\text{iso}}(r_{\text{iso}} - c_e)$ is forward invariant, i.e.,

$$\alpha(t_s) \in C_{\text{iso}}(r_{\text{iso}} - c_e) \Rightarrow \varphi^{t-t_s}(\alpha(t_s)) \in C_{\text{iso}}(r_{\text{iso}} - c_e), \quad \forall t \in [t_s, t_f] \quad (27)$$

where $\varphi^{t-t_s}(\alpha(t_s))$ is the ISO state trajectory with $\varphi^0(\alpha(t_s)) = \alpha(t_s)$ at $t = t_s$ as given in Table 2 and defined in Definition 1.

If \mathcal{J} of (16) is locally Lipschitz in x and α , k of (19) can be expressed as a composition of locally Lipschitz functions in x and α , which implies that the Lipschitz assumption (26) always holds for finite r_{iso} and r_{sc} . Since the estimation error is expected to decrease in general, c_e of Assumption 1 can be made smaller as t_s gets larger, which renders the second condition of Assumption 2 less strict (see Appendix for details in how we select c_e).

V. Neural-Rendezvous: Learning-based Robust Guidance and Control to Encounter ISOs

This section finally presents Neural-Rendezvous, a deep learning-based terminal G&C approach to autonomously encounter ISOs, thereby solving the problems (P1) and (P2) of Sec. II that arise from the large state uncertainty and high-velocity challenges. It will be shown that the SN-DNN min-norm control (18) of Lemma 2 verifies a formal exponential bound on expected spacecraft delivery error, with a finite probability and finite optimality gap, which provides valuable information in determining whether we should use the SN-DNN terminal guidance policy or enhance it with the SN-DNN min-norm control, depending on the size of the state uncertainty.

A. Robustness and Stability Guarantee

The assumptions introduced in Sec. IV.C allows bounding the mean squared distance between the spacecraft relative position of (1) controlled by (18) and the desired position $p_d(t)$ given in (15), even under the presence of the state uncertainty (see Fig. 5). We remark that the additional notations in the following theorem are summarized in Table 4, where the others are consistent with the ones in Table 3.

Theorem 2. *Suppose that Assumptions 1 and 2 hold, and that the spacecraft relative dynamics with respect to the ISO, given in (1), is controlled by $u = u_\ell^*$. If the estimated states at time $t = t_s$ satisfy $\hat{\alpha}_s \in C_{\text{iso}}(\bar{R}_{\text{iso}})$ and $\hat{x}_s \in C_{\text{sc}}(\bar{R}_{\text{sc}})$, then*

Table 4 Notations in Theorem 2.

\mathcal{D}_{est}	Set defined as $\mathcal{D}_{\text{est}} = \{(\alpha_s, x_s) \in \mathbb{R}^n \times \mathbb{R}^n \mid \sqrt{\ \alpha_s - \hat{\alpha}_s\ ^2 + \ x_s - \hat{x}_s\ ^2} \leq c_e\}$
L_k	Lipschitz constant of k in Assumption (1)
$m_{\text{sc}}(t)$	Spacecraft mass of (2) satisfying $m_{\text{sc}}(t) \in [m_{\text{sc}}(t_s), m_{\text{sc}}(t_f)]$ due to Tsiolkovsky rocket equation
$\alpha_s, \hat{\alpha}_s, x_s, \hat{x}_s$	True and estimated ISO and S/C state at time $t = t_s$, respectively
$p_d(t)$	Desired S/C relative position trajectory, i.e., $x_d(t) = [p_d(t)^\top, \dot{p}_d(t)^\top]^\top$ for x_d of (15)
p_s, \hat{p}_s	True and estimated S/C relative position at time $t = t_s$, i.e., $x_s = [p_s^\top, \dot{p}_s^\top]^\top$ and $\hat{x}_s = [\hat{p}_s^\top, \dot{\hat{p}}_s^\top]^\top$
$\bar{R}_{\text{iso}}, \bar{R}_{\text{sc}}$	Constants defined as $\bar{R}_{\text{iso}} = r_{\text{iso}} - 2c_e$ and $\bar{R}_{\text{sc}} = r_{\text{sc}} - 2c_e$ for c_e of Assumption 1 and r_{iso} and r_{sc} of Assumption 2
u_ℓ^*	SN-DNN min-norm control policy (18) of Lemma 2
$v(x, t)$	Non-negative function given as $v(x, t) = \sqrt{V(\dot{p}, \varrho_d(p, t), t)} = \sqrt{m_{\text{sc}}(t)} \ \Lambda(p - p_d(t)) + \dot{p} - \dot{p}_d(t)\ $ for V of (23)
Z_s	Tuple of true and estimated ISO and S/C state at time $t = t_s$, i.e., $Z_s = (\alpha_s, \hat{\alpha}_s, x_s, \hat{x}_s)$
α	Positive constant of (22)
$\underline{\lambda}$	Minimum eigenvalue of Λ defined in (22)
ρ	Desired terminal S/C relative position of (4)

the spacecraft delivery error is explicitly bounded as follows with probability at least $1 - \varepsilon_{\text{ctrl}}$:

$$\begin{aligned} \mathbb{E} [\|p(t_f) - \rho\| \mid \hat{\alpha}(t_s) = \hat{\alpha}_s \cap \hat{x}(t_s) = \hat{x}_s] &\leq \sup_{(\alpha_s, x_s) \in \mathcal{D}_{\text{est}}} e^{-\underline{\lambda}(t_f - t_s)} \|p_s - p_d(t_s)\| + \frac{e^{-\underline{\lambda}t_f} L_k}{m_{\text{sc}}(t_f)} \int_{t_s}^{t_f} \varpi^\tau(Z_s, t_s) d\tau \\ &+ \begin{cases} \frac{e^{-\underline{\lambda}(t_f - t_s)} - e^{-\alpha(t_f - t_s)}}{\alpha - \underline{\lambda}} \frac{v(x_s, t_s)}{\sqrt{m_{\text{sc}}(t_f)}} & \text{if } \alpha \neq \underline{\lambda} \\ (t_f - t_s) e^{-\underline{\lambda}(t_f - t_s)} \frac{v(x_s, t_s)}{\sqrt{m_{\text{sc}}(t_f)}} & \text{if } \alpha = \underline{\lambda} \end{cases} \end{aligned} \quad (28)$$

where $\varepsilon_{\text{ctrl}} \in \mathbb{R}_{\geq 0}$ is the probability given in (50) of Appendix, $\varpi^\tau(Z_s, t_s)$ is a time-varying function defined as $\varpi^\tau(Z_s, t_s) = e^{(\underline{\lambda} - \alpha)t} \int_{t_s}^t e^{\alpha\tau} \varsigma^\tau(Z_s, t_s) d\tau$. Note that (28) yields a bound on $\mathbb{P} [\|p(t_f) - \rho\| \leq d \mid \hat{\alpha}(t_s) = \hat{\alpha}_s \cap \hat{x}(t_s) = \hat{x}_s]$ as in Theorem 2.5 of [16], where $d \in \mathbb{R}_{\geq 0}$ is any given distance of interest, using Markov's inequality [72, pp. 311-312].

Proof. A complete proof of this theorem can be found in Appendix and we thus give a sketch of the proof here. The dynamics (17) controlled by (18) can be rewritten as

$$\ddot{p} = \mathcal{J}(x, \alpha, t) + \mathcal{B}(x, \alpha, t) u_\ell^*(x, \alpha, t; \theta_{\text{nn}}) + \mathcal{B}(x, \hat{\alpha}, t) \tilde{u} \quad (29)$$

where $\tilde{u} = u_\ell^*(\hat{x}, \hat{\alpha}, t; \theta_{\text{nn}}) - u_\ell^*(x, \alpha, t; \theta_{\text{nn}})$. Qualitatively speaking, since the learning-based control is constructed to make the closed-loop part $\ddot{p} = \mathcal{J}(x, \alpha, t) + \mathcal{B}(x, \alpha, t) u_\ell^*(x, \alpha, t; \theta_{\text{nn}})$ robust and exponentially stable with respect to the desired trajectory x_d of (8), we can view \tilde{u} , which arises from the ISO state uncertainty, as external disturbance to get an exponential bound on $\mathbb{E}_{Z_s} [\|p(t) - p_d(t)\|]$ as in Theorem 2.5 of [16], where $\mathbb{E}_{Z_s} [\cdot] = \mathbb{E} [\cdot \mid x(t_s) = x_s, \hat{x}(t_s) = \hat{x}_s, \alpha(t_s) = \alpha_s, \hat{\alpha}(t_s) = \hat{\alpha}_s]$. The rest follows from deriving the probability of the

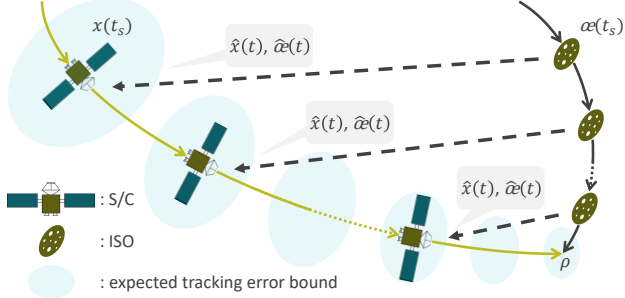


Fig. 7 Illustration of expected position tracking error bound (28) of Theorem 2, where $\varsigma^t(Z_s, t_s)$ is assumed to be non-increasing function in time.

states $\alpha(t)$, $\hat{\alpha}(t)$, $x(t)$, and $\hat{x}(t)$ remaining in the sets where the estimation bound (25) and the Lipschitz condition (26) hold for $\forall t \in [t_s, t_f]$ under Assumptions 1 and 2. \square

As derived in Theorem 2, the SN-DNN min-norm control policy (18) of Lemma 2 enhances the SN-DNN terminal guidance policy of Theorem 1 by providing the explicit spacecraft delivery error bound (28), which holds even under the presence of the state uncertainty. This bound is valuable in modulating the learning and control parameters to achieve a verifiable performance guarantee consistent with a mission-specific performance requirement as to be seen in Sec. V.C.

B. Examples and Optimality Guarantee

As illustrated in Fig. 7, the expected state tracking error bound (28) of Theorem 2 decreases exponentially in time if $\varsigma^t(Z_s, t_s)$ is a non-increasing function in t . The following examples demonstrate how we compute the bound (28) in practice.

Example 1. Suppose that the estimation error is upper-bounded by a function that exponentially decreases in time, i.e., we have $\varsigma^t(Z_s, t_s) = e^{-\beta(t-t_s)} \sqrt{\|\hat{\alpha}_s - \alpha_s\|^2 + \|\hat{x}_s - x_s\|^2} + c$ for (25) in Assumption 1 as in [39–42], where $c \in \mathbb{R}_{\geq 0}$ and $\beta \in \mathbb{R}_{>0}$. Assuming that $\alpha \neq \beta$, $\beta \neq \underline{\lambda}$, and $\underline{\lambda} \neq \alpha$ for simplicity, we get

$$\begin{aligned} \text{RHS of (28)} &\leq e^{-\underline{\lambda}\bar{t}_f} (\|\hat{p}_s - p_d(t_s)\| + c_e) + \frac{e^{-\underline{\lambda}\bar{t}_f} - e^{-\alpha\bar{t}_f}}{\alpha - \underline{\lambda}} \frac{(\bar{\lambda} + 1)(\|\hat{x}_s - x_d(t_s)\| + c_e)}{\sqrt{m_{sc}(t_f)}} \\ &+ \frac{L_k}{m_{sc}(t_f)} \left(\frac{c_e}{\alpha - \beta} \left(\frac{e^{-\underline{\lambda}\bar{t}_f} - e^{-\beta\bar{t}_f}}{\beta - \underline{\lambda}} - \frac{e^{-\underline{\lambda}\bar{t}_f} - e^{-\alpha\bar{t}_f}}{\alpha - \underline{\lambda}} \right) + \frac{c}{\alpha} \left(\frac{1 - e^{-\underline{\lambda}\bar{t}_f}}{\underline{\lambda}} - \frac{e^{-\underline{\lambda}\bar{t}_f} - e^{-\alpha\bar{t}_f}}{\alpha - \underline{\lambda}} \right) \right) \end{aligned} \quad (30)$$

where $\bar{t}_f = t_f - t_s$. Note that the bound (30) can be computed explicitly for given \hat{x}_s and $\hat{\alpha}_s$ at time $t = t_s$ as long as $\hat{\alpha}_s \in C_{iso}(\bar{R}_{iso})$ and $\hat{x}_s \in C_{sc}(\bar{R}_{sc})$. Its dominant term in (30) for large \bar{t}_f is $L_k c / (m_{sc}(t_f) \alpha \underline{\lambda})$ due to the following relation:

$$\lim_{t_f \rightarrow \infty} \text{RHS of (30)} = \frac{L_k c}{m_{sc}(t_f) \alpha \underline{\lambda}}.$$

Example 2. For the case where we can only guarantee that $\mathbb{E}_{Z_s} \left[\sqrt{\|\hat{\alpha}(t) - \alpha(t)\|^2 + \|\hat{x}(t) - x(t)\|^2} \right] \leq \bar{\sigma}$ for $\bar{\sigma} \in \mathbb{R}_{\geq 0}$ in (25) of Assumption 1, we get

$$\begin{aligned} \text{RHS of (28)} &\leq e^{-\underline{\lambda} \bar{t}_f} (\|\hat{p}_s - p_d(t)\| + \bar{\sigma}) + \frac{e^{-\underline{\lambda} \bar{t}_f} - e^{-\alpha \bar{t}_f}}{\alpha - \underline{\lambda}} \frac{(\bar{\lambda} + 1)(\|\hat{x}_s - x_d(t)\| + \bar{\sigma})}{\sqrt{m_{sc}(t_f)}} \\ &\quad + \frac{L_k c}{m_{sc}(t_f) \alpha} \left(\frac{1 - e^{-\underline{\lambda} \bar{t}_f}}{\underline{\lambda}} - \frac{e^{-\underline{\lambda} \bar{t}_f} - e^{-\alpha \bar{t}_f}}{\alpha - \underline{\lambda}} \right) \end{aligned}$$

which can be obtained using (30).

In addition to the stability and robustness property shown in Theorem 2, the SN-DNN min-norm control policy (18) of Lemma 2 possesses a finite optimality gap with respect to the optimal MPC policy of (5) as in (12) of Theorem 1, thanks to the objective function of (21).

Theorem 3. Suppose that \mathcal{f} of (16) is Lipschitz in the first two arguments with its 2-norm Lipschitz constant $L_f \in \mathbb{R}_{>0}$. The SN-DNN min-norm control policy (18) of Lemma 2 has the following bound, which reduces to the optimality gap $\epsilon_{\ell u}$ of Theorem 1 as the state tracking error and estimation error tend to zero:

$$\begin{aligned} \|u_{\ell}^*(\hat{x}(t), \hat{\alpha}(t), t; \theta_{nn}) - u_{\text{mpc}}(\hat{x}(t), \hat{\alpha}(t), t)\| &\leq \epsilon_{\ell u} + (L_{\ell} + m_{sc}(0)L_f)\|\hat{\alpha}(t) - \alpha_d(t)\| \\ &\quad + (L_{\ell} + m_{sc}(0)(L_f + \bar{\lambda}(\alpha + 1) + \alpha))\|\hat{x}(t) - x_d(t)\| \end{aligned} \quad (31)$$

where u_{mpc} is the optimal MPC policy given by (5), L_{ℓ} is the Lipschitz constant of the SN-DNN guidance policy u_{ℓ} of Theorem 1, and the other notations are given in Table 4.

Proof. Using triangle inequality, we get $\|u_{\ell}^*(\hat{x}(t), \hat{\alpha}(t), t; \theta_{nn}) - u_{\text{mpc}}(\hat{x}(t), \hat{\alpha}(t), t)\| \leq \|u_{\ell}(x_d(t), \alpha_d(t), t; \theta_{nn}) - u_{\text{mpc}}(\hat{x}(t), \hat{\alpha}(t), t)\| + \|k(\hat{x}(t), \hat{\alpha}(t), t)\|$. For the first term, the Lipschitz property of u_{ℓ} along with the result of Theorem 1 implies

$$\|u_{\ell}(x_d(t), \alpha_d(t), t; \theta_{nn}) - u_{\text{mpc}}(\hat{x}(t), \hat{\alpha}(t), t)\| \leq \epsilon_{\ell u} + L_{\ell}(\|\hat{\alpha}(t) - \alpha_d(t)\| + \|\hat{x}(t) - x_d(t)\|).$$

The second term can be bounded as follows by the definition of k given in (19) of Lemma 2

$$\|k(\hat{x}(t), \hat{\alpha}(t), t)\| \leq m_{sc}(0)L_f(\|\hat{\alpha}(t) - \alpha_d(t)\| + \|\hat{x}(t) - x_d(t)\|) + m_{sc}(0)\|\alpha \Lambda \hat{e}(t) + (\Lambda + \alpha I_{3 \times 3})\dot{\hat{e}}(t)\| \quad (32)$$

where $\hat{e}(t) = \hat{p}(t) - p_d(t)$ and the Lipschitz assumption for \mathcal{f} is also used to obtain the inequality. Bounding the last term in (32) by $m_{sc}(0)(\bar{\lambda}(\alpha + 1) + \alpha)\|\hat{x}(t) - x_d(t)\|$ gives the desired result (31). \square

Since the spacecraft delivery error (28) and the optimality gap (31) both depend on the state estimation error, which

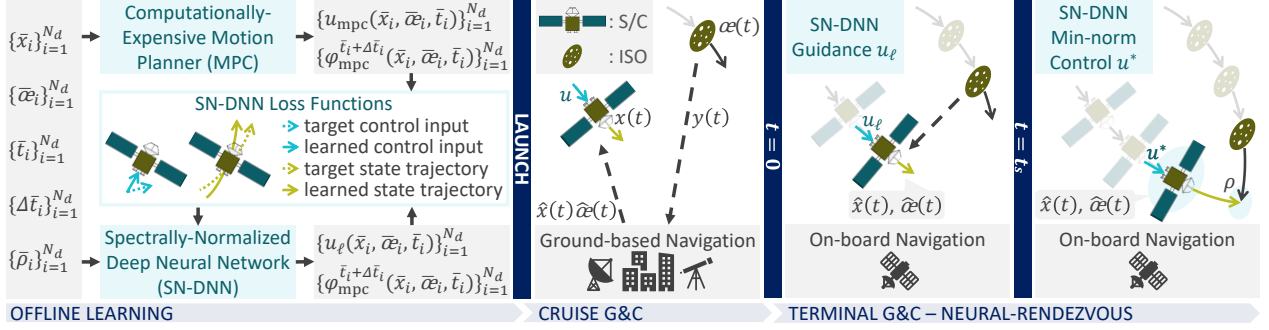


Fig. 8 Mission timeline for encountering ISO, where $y(t)$ is state measurement as in Fig. 3 and the other notation follows that of Theorems 1 and 2. Terminal G&C (Neural-Rendezvous) is performed using SN-DNN guidance and min-norm control policies online as in Algorithm 2, thereby enabling fast response autonomous operation under large ISO state uncertainty and high-velocity challenges. Note that SN-DNN is trained offline using Algorithm 1.

is expected to become smaller as the spacecraft gets closer to the ISO as mentioned in the problem (P1) of Sec. II, they can be considered as a tool to determine whether we should use the SN-DNN terminal guidance policy of Theorem 1 or the SN-DNN min-norm control policy (18) of Lemma 2, based on the trade-off between them as to be seen in the following.

C. Neural-Rendezvous

We summarize the pros and cons of the aforementioned terminal G&C techniques.

- The SN-DNN terminal guidance policy of Theorem 1, which solves the problem (P1) of Sec. II, can be implemented in real-time and possesses a small optimality gap as in (12), resulting in the near-optimal guarantee in terms of dynamic regret [10–12] as discussed below (5) and Theorem 1. However, obtaining any quantitative bound on the spacecraft delivery error with respect to the desired relative position, to either flyby or impact the ISO, is difficult in general [16, 28].
- In contrast, the SN-DNN min-norm control policy (18) of Lemma 2, which solves the problem (P2) of Sec. II, can also be implemented in real-time and provides an explicit upper-bound on the spacecraft delivery error that decreases in time as proven in Theorem (2). However, the desired trajectory it tracks is subject to the large state uncertainty initially for small t_s , resulting in a large optimality gap as can be seen from (31) of Theorem 3.

Based on these observations, it is ideal to utilize the SN-DNN terminal guidance policy without any feedback control initially for large state uncertainty, to avoid having a large optimality gap as in (31) of Theorem (3), then activate the SN-DNN min-norm control once the verifiable spacecraft delivery error of (28) of Theorem (2) becomes smaller than a mission-specific threshold value for the desired trajectory (15), which is to be updated at $t_d \in [0, t_f]$ along the way as discussed in Remark 6. The pseudo-code for the proposed learning-based approach for encountering the ISO is given in Algorithm 2, and its mission timeline is shown in Fig. 8.

Algorithm 2: Neural-Rendezvous

Inputs : u_ℓ of Theorem 1 and u_ℓ^* of Lemma 2

Outputs : Control input u of (1) for $t \in [0, t_f]$

$t_0 \leftarrow \text{current time}$

$\Delta t \leftarrow \text{control time interval}$

$t_k, t_d, t_{\text{int}} \leftarrow \text{current time} - t_0$

$\text{flagA}, \text{flagB} \leftarrow 0$

while $t_k < t_f$ **do**

 Obtain $\hat{x}(t_k)$ and $\hat{\alpha}(t_k)$ using navigation technique

if $\text{flagA} = 0$ **then**

$u \leftarrow u_\ell(\hat{x}(t_k), \hat{\alpha}(t_k), t_k)$

else

if $\text{flagB} = 1$ **then**

$u \leftarrow u_\ell^*(\hat{x}(t_k), \hat{\alpha}(t_k), t_k)$

else

 Compute RHS of (28) in Theorem 2 with $t_s = t_k$

if RHS of (28) $>$ threshold **then**

$u \leftarrow u_\ell(\hat{x}(t_k), \hat{\alpha}(t_k), t_k)$

else

$u \leftarrow u_\ell^*(\hat{x}(t_k), \hat{\alpha}(t_k), t_k)$

$\text{flagB} \leftarrow 1$

 Apply u to (1) for $t \in [t_k, t_k + \Delta t]$

while current time $- t_0 < t_k + \Delta t$ **do**

if $\text{flagB} = 0$ **then**

 Integrate dynamics to get x_d and α_d of (15) from t_{int}

if integration is complete **then**

 Update x_d and α_d

$t_d, t_{\text{int}} \leftarrow t_k + \Delta t$

$\text{flagA} \leftarrow 1$

else

$t_{\text{int}} \leftarrow \text{time when S/C stopped integration}$

$t_k \leftarrow t_k + \Delta t$

Remark 7. We use t_{int} in Algorithm 2 to account for the fact that computing x_d could take more than Δt for small Δt and t_k as pointed out in Remark 6, and thus the spacecraft is sometimes required to compute it over multiple time steps. It can be seen that the SN-DNN terminal guidance policy u_ℓ is also useful when the spacecraft does not possess x_d yet, i.e., when $\text{flagA} = 0$. Also, the impact of discretization introduced in Algorithm 2 will be demonstrated in Sec. VII.C, where the detailed discussion of its connection to continuous-time stochastic systems can be found in [73].

VI. Extensions

In this section, we present several extensions of the proposed G&C techniques for encountering ISOs, which can be used to further improve certain aspects of their performance.

A. Optimal Lyapunov Functions and Other Types of Disturbances

The Neural-Rendezvous approach in Algorithm 2 is based on the feedback control of Lemma 2, constructed using the non-negative function V of (23). In general, we can always construct such a feedback control policy as long as there exists a Lyapunov function $\mathcal{V} : \mathbb{R}^n \times \mathbb{R}^n \times \mathbb{R}_{\geq 0} \mapsto \mathbb{R}_{\geq 0}$ [70, p. 154] and control policy $u = \mu(x, \alpha, t)$ that satisfies

$$k_1 \|(x - x_d)\|^2 \leq \mathcal{V}(x, \alpha, t) \leq k_2 \|(x - x_d)\|^2 \quad (33)$$

$$\frac{\partial \mathcal{V}}{\partial t} + \frac{\partial \mathcal{V}}{\partial \alpha} \dot{\alpha} + \frac{\partial \mathcal{V}}{\partial x} (f(x, \alpha, t) + B(x, \alpha, t)\mu(x, \alpha, t)) \leq -2\alpha \mathcal{V}(x, \alpha, t) \quad (34)$$

$\forall x, \alpha \in \mathbb{R}^n$ and $t \in \mathbb{R}_{\geq 0}$, where $k_1, k_2, \alpha \in \mathbb{R}_{>0}$, and u , f , and B are given in (1). The combination of such \mathcal{V} and μ is not necessarily unique, and many studies have discussed optimal and numerically efficient ways to find them, as partially summarized in [16]. For example, contraction theory [16, 23, 74, 75] uses a squared differential length $\mathcal{V} = \delta x^\top M(x, \alpha, t) \delta x$ as a Lyapunov-like function, allowing the systematic construction of \mathcal{V} and μ of (33) and (34) via convex optimization to minimize an upper bound of the steady-state distance between the controlled and desired system trajectories [73, 75]. The computational burden of these approaches can be significantly reduced by using machine learning techniques [16, 28, 41, 42].

It is worth emphasizing that since our proposed feedback control of Lemma 2 is also categorized as a Lyapunov-based approach (which can be verified for $\mathcal{V} = V + \epsilon(p - p_d)^\top \Lambda(p - p_d)$, where V and Λ are given in (21) and $\epsilon \in \mathbb{R}_{>0}$ is as defined in [76, pp. 54-55]), we can show that it is robust not only against the state uncertainty of (1), but also deterministic and stochastic disturbances resulting from e.g., process noise, control execution error, parametric uncertainty, and unknown parts of dynamics as shown in [16, 77, 78].

B. Stochastic MPC with Terminal Chance Constraints

We could utilize the expectation bound (28) in the guidance problem to compute a risk-constrained policy using terminal chance-constrained stochastic optimal control problem formulation in [79], with probabilistic guarantees on reaching the terminal set. This approach improves the quality of the solution that is approximated by an SN-DNN as in Theorem 1. Using the same notation as in (3) of Sec. III.A, the chance-constrained stochastic optimal control problem is described as follows:

$$\begin{aligned} u^*(\hat{x}(\tau), \hat{\alpha}(\tau), t, \rho) &= \arg \min_{u(t) \in \mathcal{U}(t)} \mathbb{E} \left[\int_{\tau}^{t_f} J_S(\xi(t), u(t)) dt + J_{S_f}(\xi(t_f)) \right] \\ \text{s.t. } d\xi(t) &= f(\xi(t), \varphi^{t-\tau}(\hat{\alpha}(\tau)), t) dt + B(\xi(t), \varphi^{t-\tau}(\hat{\alpha}(\tau)), t) dt + G(\xi(t), \varphi^{t-\tau}(\hat{\alpha}(\tau)), u(t)) d\mathcal{W}(t), \forall t \in [\tau, t_f] \\ \mathbb{E}(\xi(\tau)) &= \hat{x}(\tau), x(t_f) \in \mathcal{X}_{S_f} \end{aligned} \quad (35)$$

where J_{S_f} and J_S are given transient and terminal cost functions, $G : \mathbb{R}^n \times \mathbb{R}^n \times \mathbb{R}_{\geq 0} \rightarrow \mathbb{R}^{n \times w}$ is a matrix-valued diffusion coefficient for stochastic disturbance, $\mathcal{W} : \mathbb{R}_{\geq 0} \mapsto \mathbb{R}^w$ is a w -dimensional Wiener process [80, p. 100] (see also [80, p. xii] for the notations used), and the terminal constraint set \mathcal{X}_{S_f} is defined using a quadratic chance constraint as follows:

$$\mathcal{X}_{S_f} = \{x \in \mathbb{R}^n \mid \mathbb{P}[(x - \rho)^T Q \chi_f (x - \rho) \leq c_f] \geq 1 - \epsilon_f\},$$

where $Q \chi_f > 0$, $c_f \in \mathbb{R}_{\geq 0}$, and ϵ_f is the risk measure. The terminal set defines the encounter specifications (position, velocity, and their variance, respectively) with the ISO. Unlike the formulation given in (3), the problem (35) explicitly account for the stochastic disturbance resulting from the ISO state uncertainty in its dynamics, leading to a more sophisticated offline solution that can be obtained using the generalized polynomial chaos-based sequential convex programming method [79].

C. Additional Remarks

1. Multi-Agent Systems in Cluttered Environments

The optimization formulation with chance constraints in Sec. VI.B is also useful in extending our proposed approach to a multi-agent setting with obstacles, where each spacecraft is required to achieve its mission objectives in a collision-free manner. It allows expressing stochastic guidance problems as deterministic counterparts [79] so we could exploit existing methods for designing distributed, robust, and safe control policies for deterministic multi-agent systems, which can be computed in real-time [28, 29].

2. Discrete-Time Systems

Although this paper considers a continuous-time system and we discretize it when implementing the proposed algorithm as discussed in Remark 7, where the impact of discretization is to be demonstrated in Sec. VII.C, we could also start from a discrete-time system and analyze robustness and stability in a discrete sense, which can be performed by replacing the stability constraint (34) with its discrete versions introduced in [73, 74, 81–85].

3. Robustness of Neural Networks

As discussed in Remark 4, there are several ongoing studies in the field of machine learning that view a neural network as one form of a dynamical system, so their robustness performance could be analyzed using the techniques of Lyapunov and contraction theory described in Sec. VI.A. These approaches typically rewrite a neural network as a discrete-time dynamical system, and utilize the stability constraint of Sec. VI.C.2 as either a regularization loss or a structural constraint of neural networks [62–67]. This permits us to augment them with stronger robustness and stability guarantees that could further tighten the optimality gap of Theorem 1.

4. Online Learning

The proposed learning-based algorithm is based solely on offline learning and online guarantees of robustness and stability, but there could be situations where the parametric or non-parametric uncertainty of underlying dynamical systems is too large to be treated robustly. As shown in [16], robust control techniques, including our proposed approach in this paper, can always be augmented with adaptive control techniques with formal stability [7, 9, 86–88] and with static or dynamic regret bounds [89, 90] for online nonlinear control problems [91].

VII. Simulation

Our proposed framework, Neural-Rendezvous, is demonstrated using the data set that contains ISO candidates for possible exploration [6, 17] to validate if it indeed solves Problems **(P1)** and **(P2)** introduced earlier in Sec. II. PyTorch [92] is used for designing and training neural networks and NASA’s Navigation and Ancillary Information Facility (NAIF) [93, 94] is used to obtain relevant planetary data. A YouTube video which visualizes these simulation results can be found at https://youtu.be/8h60B_p1fyQ.

A. Simulation Setup

All the G&C frameworks in this section are implemented with the control time interval 1 s unless specified, and their computational time of which is measured using the MacBook Pro laptop (2.2 GHz Intel Core i7, 16 GB 1600 MHz DDR3 RAM). The terminal time t_f of (4) for terminal guidance is selected to be $t_f = 86400$ (s), and the wet mass of the spacecraft at the beginning of terminal guidance is assumed to be 150 kg. Also, we consider the SN-DNN min-norm

control (18) of Theorem 2 designed with $\Lambda = 1.3 \times 10^{-3}$ and $\alpha = 8.9 \times 10^{-7}$. The maximum control input is assumed to be $u_{\max} = 3$ (N) in each direction with the total admissible delta-V (2-norm S/C velocity increase) being 0.6 km/s.

B. Dynamical System-Based SN-DNN Training

This section delineates how we train the dynamical system-based SN-DNN for solving the autonomous terminal guidance problem (P1) in Sec. II using Algorithm 1.

1. State Uncertainty Assumption

For the sake of simplicity, we assume that the spacecraft has access to the estimated ISO and its relative state generated by the respective normal distribution $\mathcal{N}(\mu, \Sigma)$, with μ being the true state and Σ being the navigation error covariance, where $\text{Tr}(\Sigma)$ exponentially decaying in t as in Example 1 similar to [39–42]. In particular, we assume that the standard deviations of the ISO and spacecraft absolute along-track position, cross-track position, along-track velocity, and cross-track velocity, expressed in the ECLIPJ2000 frame as in JPL’s [SPICE toolkit](#) [94], are 10^4 km, 10^2 km, 10^{-2} km/s, and 10^{-2} km/s initially at time $t = 0$ (s), and decays to $\mathcal{O}(10^1)$ km, $\mathcal{O}(10^0)$ km, $\mathcal{O}(10^{-4})$ km/s, and $\mathcal{O}(10^{-4})$ km/s finally at time $t = t_f = 86400$ (s) in the along-track and cross-track direction, respectively, which can be achieved by using, e.g., the extended Kalman filter [39] with full state measurements and estimation gains given by $R = I_{n \times n}$ and $Q = I_{n \times n} \times 10^{-10}$.

These uncertainties are derived from an autonomous optical navigation orbit determination filter, as is used in the AutoNav system [5]. A Monte-Carlo analysis simulating AutoNav performance was run to provide state estimation error versus time results. The distribution of errors at each time step then provides the input uncertainty profile.

Remark 8. *As discussed in Remark 1, G&C are the focus of our study and navigation is beyond our scope, we have simply assumed the ISO state measurement uncertainty given above following the discussion of [6]. The assumption can be easily modified accordingly to the state estimation schemes to be used in each aerospace and robotic problem of interest.*

2. Training Data Generation

We generate 499 candidate ISO and spacecraft ideal trajectories based on the ISO population given in [17] and analyzed in [6], and utilized the first 399 ISOs for training the SN-DNN and the other 100 for testing its performance later in this section. We then obtain 10000 time and ISO index pairs (t_i, I_i) uniformly and randomly from $[0, t_f] \times [1, 399] \cup \mathbb{N}$ and perturbed the ISO and spacecraft ideal state with the uncertainty given in Sec. VII.B.1 to produce the training samples $(\bar{x}_i, \bar{w}_i, \bar{t}_i)$ of Algorithm 1 for the control input loss (i.e., the first term of (9)). The training data samples for the state trajectory loss (i.e., the second term of (9)) are obtained in the same way using the pairs generated uniformly and randomly from $[0, 3600] \times [1, 399] \cup \mathbb{N}$, with $\Delta \bar{t}_i$ of Algorithm 1 fixed to $\Delta \bar{t}_i = 10$ (s). The desired relative positions $\bar{\rho}_i$

in (10) are also sampled uniformly and randomly from the surface of a ball with radius 100 km.

The desired control inputs $u_{\text{mpc}}(\bar{x}_i, \bar{\alpha}_i, \bar{t}_i, \bar{\rho}_i)$ and desired state trajectories $\varphi_{\text{mpc}}^{\bar{t}_i + \Delta \bar{t}_i}(\bar{x}_i, \bar{\alpha}_i, \bar{t}_i, \bar{\rho}_i)$ of Algorithm 1 are then sampled by solving (5) using the sequential convex programming approach [45–47] and by numerically integrating (8) using the fourth-order Runge–Kutta method, respectively, where the terminal position error is treated as a constraint $\|p_\xi(t_f) - \rho\| = 0$ in (4), the cost function of (3) is defined with $c_0 = 0$, $c_1 = 1$, and $P(u(t), \xi(t)) = \|u(t)\|^2$ as in Remark 2, and the control input constraint $u(t) \in \mathcal{U}(t) = \{u \in \mathbb{R}^m \mid |u_i| \leq u_{\max}\}$ u_i is used with u_i being the i th element of u and $u_{\max} = 3$ (N). Note that the problem is discretized with the time step 1 s, consistently with the control time interval.

3. Training Data Normalization

Instead of naively training the SN-DNN with the raw data generated in Sec. VII.B.2, we transform the SN-DNN input data $(\bar{x}_i, \bar{\alpha}_i, \bar{t}_i, \bar{\rho}_i)$ as follows, thereby accelerating the speed of learning process and improving neural network generalization performance:

$$\text{SN-DNN input} = \left(\bar{p}_i - \bar{\rho}_i, \frac{\bar{p}_i - \bar{\rho}_i}{t_f - \bar{t}_i} + \dot{\bar{p}}_i, \bar{\rho}_i, t_f - \bar{t}_i, \bar{\omega}_{z,i}, G(\bar{p}_i, \bar{\alpha}_i) \right) \quad (36)$$

where $\bar{x}_i = [\bar{p}_i^\top, \dot{\bar{p}}_i^\top]^\top$, $G(p, \alpha)$ is given in (2), and $\bar{\omega}_{z,i}$ is the i th training sample of the orbital element ω_z given in [15, 38], which is the dominant element of the matrix function $C(\alpha)$ of (2). We further normalize the input (36) and output $u_\ell(x, \alpha, t, \rho; \theta_{\text{nn}})$ of the SN-DNN by dividing them by their maximum absolute values in their respective training data.

4. SN-DNN Configuration and Training

We select the number of hidden layers and neurons of the SN-DNN as 6 and 64 as a result of the performance analysis similar to [41, 42], with the spectral normalization constant C_{nn} of Definition 2 being $C_{nn} = 25$. The activation function is selected to be tanh, which is also used in the last layer not to violate the input constraint $u(t) \in \mathcal{U}(t) = \{u \in \mathbb{R}^m \mid |u_i| \leq u_{\max}\}$ u_i by design. Figure 9 shows the terminal spacecraft position error (delivery error) and control effort (total delta-V) of the SN-DNN terminal guidance policy trained for 10000 epochs using several different weights $c_u, c_x \in \mathbb{R}_{\geq 0}$ of the loss function (9) in Sec. III, where its weight matrices are given as $C_x = c_x \text{diag}(\mathbf{I}_{3 \times 3}, 10^7 \times \mathbf{I}_{3 \times 3})$ and $C_u = c_u \mathbf{I}_{3 \times 3}$. The results are averaged over 50 simulations for the ISOs in the test set without any state uncertainty. Consistently with the definition of (9), this figure indicates that

- as c_x/c_u gets smaller, the loss function (9) penalizes the imitation loss of the control input more heavily than that of the state trajectory, and thus the spacecraft yields smaller control effort but with larger delivery error, and
- as c_x/c_u gets larger, the loss function (9) penalizes the imitation loss of the state trajectory more heavily than that

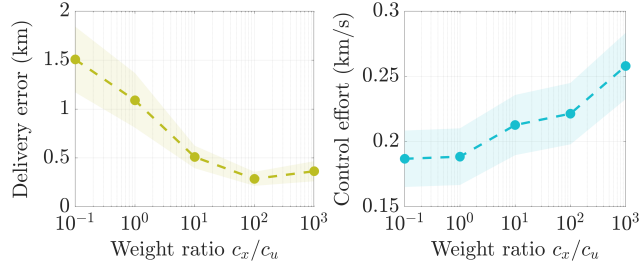


Fig. 9 Control performances versus weight ratio of SN-DNN loss function. Shaded area denotes standard deviations ($\pm 2.5 \times 10^{-1}\sigma$ for spacecraft delivery error and $\pm 5 \times 10^{-2}\sigma$ for control effort).

of the control input, and thus the spacecraft yields smaller delivery error but with larger control effort.

The weight ratio c_x/c_u of the SN-DNN to be implemented in the next section is selected as $c_x/c_u = 10^2$, which achieves the smallest delivery error with the smallest standard deviation of all the weight ratios in Fig. 9, while having the control effort smaller than the admissible delta-V of 0.6 km/s. Note that we could further optimize the ratio with the delta-V constraint based on this trade-off discussed above, but this is left as future work. The SN-DNN is then trained using SGD [50, 51] for 10000 epochs with 10000 training data points obtained as in Sec. VII.B.2, following the pseudo-code outlined in Algorithm 1.

C. Neural-Rendezvous Performance

Figure 10 shows the spacecraft delivery error and control effort of Neural-Rendezvous of Algorithm 2, SN-DNN terminal guidance of Algorithm 1, PD and robust nonlinear tracking control of [18, pp. 397-402] with respect to a pre-computed and fixed desired trajectory, and MPC with linearized dynamics [19], where the SN-DNN min-norm control (18) of Theorem 2 is activated at time $t = t_s = 26400$ (s). It can be seen that Neural-Rendezvous achieves ≤ 0.2 km delivery error for 99 % of the ISOs in the test set, even under the presence of the large ISO state uncertainty given in Sec. VII.B.1. Also, its error is indeed less than the dominant term of the expectation bound on the tracking error (28) of Theorem 2, which is computed assuming the estimation error is upper-bounded by a function that exponentially decreases in time as in Example 1. Furthermore, the SN-DNN terminal guidance can also achieve ≤ 1 km delivery error for 86 % of the ISOs, and as expected from the optimality gaps given in (12) of Theorem 1 and (31) of Theorem 3, the control effort of Neural-Rendezvous is larger than that of the SN-DNN guidance and MPC with linearized dynamics, but it is still less than the admissible delta-V of 0.6 km/s for all the ISOs in the test set.

Figure 11 then shows the spacecraft delivery error and control effort of Neural-Rendezvous of Algorithm 2 and SN-DNN terminal guidance of Algorithm 1, averaged over 100 ISOs in the test set, versus the control time interval. Although both of these methods involve discretization when implementing them in practice as pointed out in Remark 7, it can be seen that Neural-Rendezvous enables having the delivery error smaller than 5 km with its standard deviation always smaller than that of the SN-DNN guidance, even for the control interval 600 s (10 min). Since the MPC problem

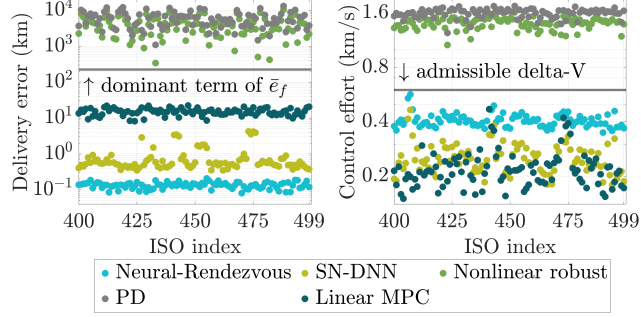


Fig. 10 Control performances versus ISOs in test set (400-499), where \bar{e}_f is right-hand side of bound (28) in Theorem 2, admissible delta-V (2-norm S/C velocity increase during terminal guidance) is assumed to be 0.6 km/s, and each result shown above is average of 10 simulations performed for each ISO.

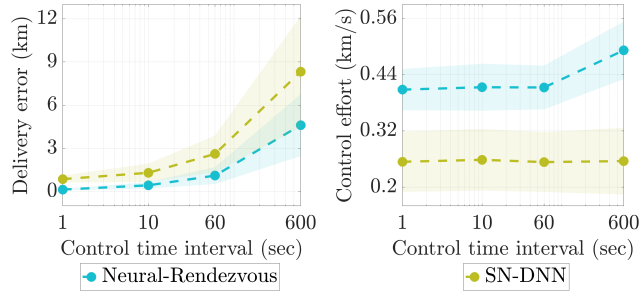


Fig. 11 Control performances versus control time interval, where each result shown above is average of 10 simulations performed for all 100 ISOs in test set (400-499). Shaded area denotes standard deviations ($\pm 1\sigma$ both for spacecraft delivery error and control effort).

is solved by discretizing it with the time step 1 s as explained in Sec. VII.B.2, and the SN-DNN min-norm control (18) of Theorem 2 is designed for continuous dynamics, Neural-Rendezvous yields less optimal control inputs for larger control time intervals, resulting in larger delivery error and control effort as expected from [73].

Finally, as shown in Table 5, we can see that all the methods presented in this section, including our proposed approaches, can be computed in ≤ 1 (s) and thus can be implemented in real-time. The observations so far imply that the proposed approach indeed provides one of the promising solutions to Problems (P1) and (P2) of Sec. II.

Table 5 Computational time of each method for ISO encounter averaged over 100 evaluations.

	Computational time (s)
Neural-Rendezvous	8.0×10^{-4}
SN-DNN	5.7×10^{-5}
Nonlinear robust control	1.2×10^{-4}
PD control	4.3×10^{-5}
Lienar approx. MPC	1.5×10^{-4}

VIII. Conclusion

This paper proposes Neural-Rendezvous – a deep learning-based terminal G&C framework for achieving ISO encounter under large state uncertainty and high-velocity challenges, where we develop a minimum-norm tracking controller with an optimal MPC-based guidance policy imitated by a spectrally-normalized deep neural network. As derived in Theorems 1–3 and illustrated in Fig. 4–8, its major advantages include 1) stability and robustness guarantees, resulting in a spacecraft delivery error bound that decreases exponentially in expectation with a finite probability; and 2) real-time performance guarantees with a verifiable optimality gap. The simulation results validate these guarantees for some possible ISO candidates visiting our solar system, which also implies that our proposed method should work for long-period comets, drones, and other fast-moving objects in robotics and aerospace applications.

Appendix

Proof of Lemma 2. Let $u_n(\hat{x}, \hat{\alpha}, t)$ be defined as follows:

$$u_n(\hat{x}, \hat{\alpha}, t) = M(t)\dot{\varrho}_d(\hat{p}, t) + C(\hat{\alpha})\varrho_d(\hat{p}, t) + G(\hat{p}, \hat{\alpha}) - \alpha M(t)(\dot{\hat{p}} - \varrho_d(\hat{p}, t))$$

where ϱ_d is as given in (20). Substituting this into the left-hand side of (22) as $u = u_n(\hat{x}, \hat{\alpha}, t)$ gives

$$2(\dot{\hat{p}} - \varrho_d(\hat{p}, t))^\top(-C(\hat{\alpha}) - \alpha M(t))(\dot{\hat{p}} - \varrho_d(\hat{p}, t)) = -2\alpha V(\dot{\hat{p}}, \varrho_d(\hat{p}, t), t)$$

where \mathcal{J} of (16) is computed with (2), and the equality follows from the skew-symmetric property of C , i.e., $C(\hat{\alpha}) + C(\hat{\alpha})^\top = \mathbf{0}_{3 \times 3}$ [15, 38]. The relation indeed indicates that $u = u_n(\hat{x}, \hat{\alpha}, t)$ is a feasible solution to the optimization problem (21). Furthermore, applying the KKT condition [48, pp. 243-244] to (21), we have that

$$\mu_{\text{KKT}}((\dot{\hat{p}} - \varrho_d(\hat{p}, t))^\top(u^*(\hat{x}, \hat{\alpha}, t; \theta_{\text{nn}}) - u_\ell(x_d(t), \alpha_d(t), t; \theta_{\text{nn}})) + \Upsilon(\hat{x}, \hat{\alpha}, t)) = 0$$

$$u^*(\hat{x}, \hat{\alpha}, t; \theta_{\text{nn}}) - u_\ell(x_d(t), \alpha_d(t), t; \theta_{\text{nn}}) + \mu_{\text{KKT}}(\dot{\hat{p}} - \varrho_d(\hat{p}, t)) = \mathbf{0}_{m \times 1}$$

for $\mu_{\text{KKT}} \in \mathbb{R}_{\geq 0}$. Solving them for $u^*(\hat{x}, \hat{\alpha}, t; \theta_{\text{nn}})$ and μ_{KKT} yields (18). Also, we get the condition $\Upsilon(\hat{x}, \hat{\alpha}, t) \leq 0$ by substituting V of (23) and \ddot{p} into the stability condition (22) with $u = u_\ell(x_d(t), \alpha_d(t), t; \theta_{\text{nn}})$. \square

Proof of Theorem 2. Since the third term of (29) is subject to stochastic disturbance due to the state uncertainty of Assumption 1, we consider the weak infinitesimal operator \mathcal{A} given in [71, p. 9], instead of taking the time derivative, for analyzing the time evolution of the non-negative function v defined as $v(x, t) = \sqrt{V(\dot{p}, \varrho_d(\dot{p}, t), t)} = \sqrt{m_{\text{sc}}(t)}\|\Lambda(p - p_d(t)) + \dot{p} - \dot{p}_d(t)\|$ for V of (23). To this end, let us compute the following time increment of v

evaluated at the true state and time (x, α, t) :

$$\Delta v = v(x(t + \Delta t), t + \Delta t) - v(x, t) = \frac{1}{2v(x, t)} \left(\frac{\partial V}{\partial p} \ddot{p}(t) + \frac{\partial V}{\partial \varrho_d} \ddot{\varrho}_d(p(t), t) + \frac{\partial V}{\partial t} \right) \Delta t + O(\Delta t^2) \quad (37)$$

where $\Delta t \in \mathbb{R}_{\geq 0}$ and the arguments $(\dot{p}(t), \varrho_d(p, t), t)$ of the partial derivatives of V are omitted for notational convenience. Dropping the argument t for the state variables for simplicity, the dynamics decomposition (29) gives

$$\begin{aligned} \frac{\partial V}{\partial \dot{p}} \ddot{p} + \frac{\partial V}{\partial \varrho_d} \ddot{\varrho}_d(p, t) + \frac{\partial V}{\partial t} &\leq \frac{\partial V}{\partial \dot{p}} (\mathcal{F}(x, \alpha, t) + \mathcal{B}(x, \alpha, t)u^*(\hat{x}, \hat{\alpha}, t; \theta_{\text{nn}})) + \frac{\partial V}{\partial \varrho_d} (\ddot{p}_d - \Lambda(\dot{p} - \dot{p}_d)) \\ &\leq -2\alpha V(\dot{p}, \varrho_d(p, t), t) + 2\frac{\partial V}{\partial \dot{p}} \mathcal{B}(x, \alpha, t) \tilde{u} = -2\alpha v(x, t)^2 + 2v(x, t) \frac{\|\tilde{u}\|}{\sqrt{m_{\text{sc}}(t)}} \end{aligned} \quad (38)$$

where the first inequality follows from the fact that the spacecraft mass $m_{\text{sc}}(t)$, described by the Tsiolkovsky rocket equation, is a decreasing function and thus $\partial V/\partial t \leq 0$, and the second inequality follows from the stability condition (22) evaluated at (x, α, t) , which is guaranteed to be feasible due to Lemma 2. Since u^* is assumed to be Lipschitz as in (26) of Assumption 2, we get the following relation for any $x_s, \hat{x}_s \in C_{\text{sc}}(r_{\text{sc}})$, $\alpha_s, \hat{\alpha}_s \in C_{\text{iso}}(r_{\text{iso}})$, and $t_s \in [0, t_f]$, by substituting (38) into (37):

$$\mathcal{A}v(x_s, t_s) = \lim_{\Delta t \downarrow 0} \frac{\mathbb{E}_{Z_s} [\Delta v]}{\Delta t} \leq -\alpha v(x_s, t_s) + \frac{L_k}{\sqrt{m_{\text{sc}}(t_f)}} \sqrt{\|\hat{\alpha}_s - \alpha_s\|^2 + \|\hat{x}_s - x_s\|^2} \quad (39)$$

where $Z_s = (x_s, \hat{x}_s, \alpha_s, \hat{\alpha}_s)$, $\mathbb{E}_{Z_s} [\cdot] = \mathbb{E} [\cdot | x(t_s) = x_s, \hat{x}(t_s) = \hat{x}_s, \alpha(t_s) = \alpha_s, \hat{\alpha}(t_s) = \hat{\alpha}_s]$, and the relation $m_{\text{sc}}(t) \geq m_{\text{sc}}(t_f)$ by the Tsiolkovsky rocket equation is also used to obtain the inequality. Applying Dynkin's formula [71, p. 10] to (39) gives the following with probability at least $1 - \varepsilon_{\text{est}}$ due to (25) of Assumption 1:

$$\mathbb{E}_{Z_s} [\|\Lambda(p(t) - p_d(t)) + \dot{p}(t) - \dot{p}_d(t)\|] \leq \frac{e^{-\alpha(t-t_s)} v(x_s, t_s)}{\sqrt{m_{\text{sc}}(t_f)}} + \frac{e^{-\alpha t} L_k}{m_{\text{sc}}(t_f)} \int_{t_s}^t e^{\alpha \tau} \varsigma^\tau(Z_s, t_s) d\tau, \quad \forall t \in [t_s, \bar{t}_e] \quad (40)$$

where $\varsigma^\tau(Z_s, t_s)$ is as given in (25) and \bar{t}_e is defined as $\bar{t}_e = \min\{t_e, t_f\}$, with t_e being the first exit time that any of the states leaves their respective set, i.e.,

$$t_e = \inf \{t \geq t_s : \alpha(t) \notin C_{\text{iso}}(r_{\text{iso}}) \cup \hat{\alpha}(t) \notin C_{\text{iso}}(r_{\text{iso}}) \cup x(t) \notin C_{\text{sc}}(r_{\text{sc}}) \cup \hat{x}(t) \notin C_{\text{sc}}(r_{\text{sc}})\}. \quad (41)$$

given that the event of (24) in Assumption 1 has occurred. Since we further have that $\mathcal{A}\|p - p_d\| = \frac{d}{dt}\|p - p_d\| \leq \|\tilde{\varrho}\| - \underline{\lambda}(p - p_d)$ for $\tilde{\varrho} = \Lambda(p - p_d) + \dot{p} - \dot{p}_d$ due to the hierarchical structure of $\tilde{\varrho}$, utilizing Dynkin's formula one

more time and then substituting (40) result in

$$\mathbb{E}_{Z_s} [\|p(t) - p_d(t)\|] \leq e^{-\underline{\lambda}(t-t_s)} \|p_s - p_d(0)\| + e^{-\underline{\lambda}t} \int_{t_s}^t \frac{e^{(\underline{\lambda}-\alpha)\tau+\alpha t_s} v(x_s, t_s)}{\sqrt{m_{sc}(t_f)}} + \frac{L_k}{m_{sc}(t_f)} \varpi^\tau(Z_s, t_s) d\tau, \forall t \in [0, \bar{t}_e] \quad (42)$$

where $x_s = [p_s^\top, \dot{p}_s^\top]^\top$.

What is left to show is that we can achieve $t_e > t_f$ with a finite probability for the first exit time t_e of (41). For this purpose, we need the following lemma.

Lemma 3. *Suppose that the events of Assumption 1 has occurred, i.e., the event of (24) has occurred and the 2-norm estimation error satisfies $\sqrt{\|\hat{\alpha}(t) - \alpha(t)\|^2 + \|\hat{x}(t) - x(t)\|^2} < c_e$ for $\forall t \in [t_s, t_f]$. If Assumption 2 holds and if we have*

$$\mathcal{A}v(x_s, t_s) \leq -\alpha v(x_s, t_s) + \frac{L_k}{\sqrt{m_{sc}(t_f)}} \sqrt{\|\hat{\alpha}_s - \alpha_s\|^2 + \|\hat{x}_s - x_s\|^2} \quad (43)$$

for any $x_s, \hat{x}_s \in C_{sc}(r_{sc})$, $\alpha_s, \hat{\alpha}_s \in C_{iso}(r_{iso})$, and $t_s \in [0, t_f]$ as in (39), then we get the following probabilistic bound for $\exists \varepsilon_{\text{exit}} \in \mathbb{R}_{\geq 0}$:

$$\mathbb{P}_{Z_s} \left[\bigcap_{t \in [t_s, t_f]} x(t) \in C_{sc}(\bar{r}_{sc}) \right] \geq 1 - \varepsilon_{\text{exit}} = \begin{cases} \left(1 - \frac{E_s}{\bar{v}}\right) e^{-\frac{H(t_f)}{\bar{v}}} & \text{if } \bar{v} \geq \frac{\sup_{t \in [t_s, t_f]} h(t)}{\bar{\alpha}} \\ 1 - \frac{\bar{\alpha} E_s + (e^{\bar{H}(t_f)} - 1) \sup_{t \in [t_s, t_f]} h(t)}{\bar{\alpha} \bar{v} e^{\bar{H}(t_f)}} & \text{otherwise} \end{cases} \quad (44)$$

where $Z_s = (\alpha_s, \hat{\alpha}_s, x_s, \hat{x}_s)$ denotes the states at time $t = t_s$, which satisfy $\alpha_s \in C_{iso}(\bar{r}_{iso})$, $\hat{\alpha}_s \in C_{iso}(\bar{R}_{iso})$, $x_s \in C_{sc}(\bar{r}_{sc})$, and $\hat{x}_s \in C_{sc}(\bar{R}_{sc})$ for $\bar{r}_{iso} = r_{iso} - c_e \geq 0$, $\bar{R}_{iso} = r_{iso} - 2c_e \geq 0$, $\bar{r}_{sc} = r_{sc} - c_e \geq 0$, and $\bar{R}_{sc} = r_{sc} - 2c_e \geq 0$, $E_s = v(x_s, t_s) + \delta_p \|p_s - p_d(t_s)\|$, $H(t) = \int_{t_s}^t h(\tau) d\tau$, $\bar{H}(t) = 2H(t)\bar{\alpha}/\sup_{t \in [t_s, t_f]} h(t)$, and $h(t) = L_k \varsigma^t(Z_s, t_s)/\sqrt{m_{sc}(t_f)}$. The suitable choices of $\bar{v}, \bar{\alpha}, \delta_p \in \mathbb{R}_{>0}$ are to be defined below.

Proof of Lemma 3. Let us define a non-negative and continuous function $E(x, t)$ as

$$E(x, t) = v(x, t) + \delta_p \|p - p_d(t)\| \quad (45)$$

where $x = [p^\top, \dot{p}^\top]^\top$ and $\delta_p \in \mathbb{R}_{>0}$. Note that $E(x, t)$ of (45) is 0 only when $x = x_d(t)$. Since we have $\mathcal{A}\|p - p_d(t)\| \leq v(x, t)/\sqrt{m_{sc}(t_f)} - \underline{\lambda}\|p - p_d(t)\|$, designing δ_p to have $\alpha - \delta_p/\sqrt{m_{sc}(t_f)} > 0$, the relation (43) gives

$$\mathcal{A}E(x_s, t_s) \leq -\bar{\alpha}E(x_s, t_s) + \frac{L_k}{\sqrt{m_{sc}(t_f)}} \sqrt{\|\hat{\alpha}_s - \alpha_s\|^2 + \|\hat{x}_s - x_s\|^2} \quad (46)$$

for any $x_s, \hat{x}_s \in C_{sc}(r_{sc})$, $\alpha_s, \hat{\alpha}_s \in C_{iso}(r_{iso})$, and $t_s \in [0, t_f]$, where $\bar{\alpha} = \min \{\alpha - \delta_p/\sqrt{m_{sc}(t_f)}, \underline{\lambda}\} > 0$. Let us define

another non-negative and continuous function $W(x, t)$ as

$$W(x, t) = E(x, t)e^{\gamma H(t)} + \frac{e^{\gamma H(t_f)} - e^{\gamma H(t)}}{\gamma}$$

where γ is a positive constant that satisfies $2\bar{\alpha} \geq \gamma \sup_{t \in [0, t_f]} h(t)$. If $\bar{v}, \bar{w} \in \mathbb{R}_{>0}$ is selected to have $W(x, t) < \bar{w} \Rightarrow E(x, t) < \bar{v} \Rightarrow x \in C_{\text{sc}}(\bar{r}_{\text{sc}}) = \bigcup_{t \in [0, t_f]} \{s \in \mathbb{R}^n \mid \|s - x_d(t)\| < \bar{r}_{\text{sc}}\} \subset \mathbb{R}^n$, which is always possible since $E(x, t)$ of (45) is 0 only when $x = x_d(t)$, then we can utilize (46) to compute $\mathcal{A}W$ as follows for any $x_s = [p_s^\top, \dot{p}_s^\top]^\top \in C_{\text{sc}}(\bar{r}_{\text{sc}})$ and $t_s \in [0, t_f]$ that satisfies $W(x_s, t_s) < \bar{w}$:

$$\mathcal{A}W(x_s, t_s) = (\gamma h(t_s)E(x_s, t_s) + \mathcal{A}E(x_s, t_s))e^{\gamma H(t_s)} - h(t_s)e^{\gamma H(t_s)} \leq (\mathcal{A}(\alpha_s, \hat{\alpha}_s, x_s, \hat{x}_s) - h(t_s))e^{\gamma H(t_s)} \quad (47)$$

where $\mathcal{A}(\alpha_s, \hat{\alpha}_s, x_s, \hat{x}_s) = L_k \sqrt{(\|\hat{\alpha}_s - \alpha_s\|^2 + \|\hat{x}_s - x_s\|^2)/m_{\text{sc}}(t_f)}$ and the inequality follows from the relation $\bar{\alpha} \geq \gamma \sup_{t \in [0, t_f]} h(t)$. Applying Dynkin's formula [71, p. 10] to (47), it can be verified that $W(x(t), t)$ is a non-negative supermartingale due to the fact that $\mathbb{E}_{Z_s} [\mathcal{A}(\alpha(t), \hat{\alpha}(t), x(t), \hat{x}(t))] \leq L_k S^t(Z_s, t_s)/\sqrt{m_{\text{sc}}(t_f)} = h(t)$ by definition of $S^t(Z_s, t_s)$ in (25) of Assumption 1, which gives the following due to Ville's maximal inequality [71, p. 26]:

$$\mathbb{P}_{Z_s} \left[\sup_{t \in [t_s, t_f]} W(x(t), t) \geq \bar{w} \right] \leq \frac{E_s + \gamma^{-1}(e^{\gamma H(t_f)} - 1)}{\bar{w}} \quad (48)$$

as long as we have $\alpha(t), \hat{\alpha}(t) \in C_{\text{iso}}(r_{\text{iso}})$ and $\hat{x}(t) \in C_{\text{sc}}(r_{\text{sc}})$ for $\forall t \in [t_s, t_f]$, where $Z_s = (\alpha_s, \hat{\alpha}_s, x_s, \hat{x}_s)$ is as defined in (44). For Z_s satisfying $\alpha_s \in C_{\text{iso}}(\bar{r}_{\text{iso}})$, $\hat{\alpha}_s \in C_{\text{iso}}(\bar{R}_{\text{iso}})$, $x_s \in C_{\text{sc}}(\bar{r}_{\text{sc}})$, and $\hat{x}_s \in C_{\text{sc}}(\bar{R}_{\text{sc}})$, the occurrence of the events of Assumption 1 and the forward invariance condition of (27) of Assumption 2 ensure that if we have $x(t) \in C_{\text{sc}}(\bar{r}_{\text{sc}})$ for $\forall t \in [t_s, t_f]$, we get $\alpha(t) \in C_{\text{iso}}(\bar{r}_{\text{iso}})$, $\hat{\alpha}(t) \in C_{\text{iso}}(r_{\text{iso}})$, and $\hat{x}(t) \in C_{\text{sc}}(r_{\text{sc}})$ for $\forall t \in [t_s, t_f]$. Therefore, selecting the constants γ and \bar{w} in the inequality (48) as in [71, pp. 82-83] yields (44) due to the relation $W(x, t) < \bar{w} \Rightarrow E(x, t) < \bar{v} \Rightarrow x \in C_{\text{iso}}(\bar{r}_{\text{iso}})$. \square

Now, let us select c_e of Assumption 1 as $c_e = k_e \mathbb{E}[S^{t_s}(Z_0, 0)]$, where Z_0 is the tuple of the true and estimated ISO and spacecraft states at time $t = 0$ and $k_e \in \mathbb{R}_{>0}$. Using Markov's inequality [72, pp. 311-312] along with the bounds (24) and (25) of Assumption 1, we get the following probability bound:

$$\mathbb{P} \left[\sqrt{\|\hat{\alpha}_s - \alpha_s\|^2 + \|\hat{x}_s - x_s\|^2} < k_e \mathbb{E}[S^{t_s}(Z_0, 0)] \right] \geq (1 - \varepsilon_{\text{est}}) \left(1 - \frac{1}{k_e} \right). \quad (49)$$

Since we have $\hat{\alpha}_s \in C_{\text{iso}}(\bar{R}_{\text{iso}})$ and $\hat{x}_s \in C_{\text{sc}}(\bar{R}_{\text{sc}})$ by the theorem assumption, the occurrence of the event in (49) implies $\alpha_s \in C_{\text{iso}}(\bar{r}_{\text{iso}})$ and $x_s \in C_{\text{sc}}(\bar{r}_{\text{sc}})$ for $\bar{r}_{\text{iso}} = r_{\text{iso}} - k_e \mathbb{E}[S^{t_s}(Z_0, 0)] \geq 0$, $\bar{r}_{\text{sc}} = r_{\text{sc}} - k_e \mathbb{E}[S^{t_s}(Z_0, 0)] \geq 0$, and then $\alpha(t) \in C_{\text{iso}}(\bar{r}_{\text{iso}})$, $\forall t \in [t_s, t_f]$ due to the forward invariance condition (27) in Assumption 2. Therefore, using ε_{err} of

Assumption 1 along with the result of Lemma 3, we have $\exists \varepsilon_{\text{ctrl}} \in \mathbb{R}_{\geq 0}$ s.t.

$$\mathbb{P} [\mathcal{A} | \hat{\alpha}(t_s) = \hat{\alpha}_s \cap \hat{x}(t_s) = \hat{x}_s] \geq 1 - \varepsilon_{\text{ctrl}} = (1 - \varepsilon_{\text{exit}})(1 - \varepsilon_{\text{est}})(1 - \varepsilon_{\text{err}}) \left(1 - \frac{1}{k_e}\right) \quad (50)$$

where $\mathcal{A} = \bigcap_{t \in [t_s, t_f]} \alpha(t) \in C_{\text{iso}}(\bar{r}_{\text{iso}}) \cap \hat{\alpha}(t) \in C_{\text{iso}}(r_{\text{iso}}) \cap x(t) \in C_{\text{sc}}(\bar{r}_{\text{sc}}) \cap \hat{x}(t) \in C_{\text{sc}}(r_{\text{sc}}) \cap \mathcal{E}$ with \mathcal{E} being the event of (24) in Assumption 1. The desired relation (28) follows by evaluating the first term of the integral in (42), and by observing that if \mathcal{A} of (50) occurs, we have $t_e > t_f$ and $\sqrt{\|\hat{\alpha}_s - \alpha_s\|^2 + \|\hat{x}_s - x_s\|^2} < k_e \mathbb{E} [S^{t_s}(Z_0, 0)]$ due to (49).

Note that if $\mathcal{E}_{\text{iso}} = \mathcal{E}_{\text{sc}} = \mathbb{R}^n$ in Assumption 1 and k is globally Lipschitz in Assumption 2, the estimation bound (25) and the Lipschitz bound (26) always hold without the second condition of Assumption 1. This indicates that the bound (28) holds as long as $(\alpha_s, x_s) \in \mathcal{D}_{\text{est}}$ for given $\hat{\alpha}_s, \hat{x}_s \in \mathbb{R}^n$, which occurs with probability at least $1 - k_e^{-1}$ due to (49). \square

Funding Sources

This work is funded by the NASA Jet Propulsion Laboratory, California Institute of Technology.

Acknowledgments

We thank Stefano Campagnola (NASA JPL) for providing his useful simulation codes utilized in Sec. VII, and thank Julie Castillo-Rogez (NASA JPL), Fred Y. Hadaegh (NASA JPL), and Karen Meech (University of Hawaii), and Robert Jedicke (University of Hawaii) for their insightful inputs and technical discussions.

References

- [1] Raymond, S. N., Armitage, P. J., Veras, D., Quintana, E. V., and Barclay, T., “Implications of the Interstellar Object 1I/’Oumuamua for Planetary Dynamics and Planetesimal Formation,” *Monthly Notices Royal Astron. Soc.*, Vol. 476, No. 3, 2018, pp. 3031–3038.
- [2] Meech, K. J., Weryk, R., Micheli, M., Kleyna, J. T., Hainaut, O. R., Jedicke, R., Wainscoat, R. J., Chambers, K. C., Keane, J. V., Petric, A., Denneau, L., Magnier, E., Berger, T., Huber, M. E., Flewelling, H., Waters, C., Schunova-Lilly, E., and Chastel, S., “A Brief Visit From a Red and Extremely Elongated Interstellar Asteroid,” *Nature*, Vol. 552, No. 7685, 2017, pp. 378–381.
- [3] Guzik, P., Drahus, M., Rusek, K., et al., “Initial Characterization of Interstellar Comet 2I/Borisov,” *Nature Astron.*, Vol. 4, 2020.
- [4] Castillo-Rogez, J., and Meech, K., “Mission Design Study for Objects on Oort Cloud Comet Orbits,” *Community White Papers Planet. Sci. Decadal Surv.*, 2020.
- [5] Riedel, J., et al., “Autonomous Optical Navigation (AutoNav) DS1 Technology Validation Report,” *NASA JPL, Caltech*, 2000.
- [6] Mages, D., Landau, D., Donitz, B., and Bhaskaran, S., “Navigation Evaluation for Fast Interstellar Object Flybys,” *Acta Astronautica*, Vol. 191, 2022, pp. 359–373.

[7] Shi, G., Shi, X., O'Connell, M., Yu, R., Azizzadenesheli, K., Anandkumar, A., Yue, Y., and Chung, S.-J., "Neural Lander: Stable Drone Landing Control using Learned Dynamics," *IEEE ICRA*, 2019, pp. 9784–9790.

[8] Shi, G., Höning, W., Shi, X., Yue, Y., and Chung, S.-J., "Neural-swarm2: Planning and Control of Heterogeneous Multirotor Swarms using Learned Interactions," *IEEE Trans. Robot.*, 2021, pp. 1–17.

[9] O'Connell, M., Shi, G., Shi, X., Azizzadenesheli, K., Anandkumar, A., Yue, Y., and Chung, S.-J., "Neural-Fly Enables Rapid Learning for Agile Flight in Strong Winds," *Sci. Robot.*, Vol. 7, No. 66, 2022, p. eabm6597.

[10] Yu, C., Shi, G., Chung, S.-J., Yue, Y., and Wierman, A., "The Power of Predictions in Online Control," *Adv. Neural Inf. Process. Syst.*, Vol. 33, 2020, pp. 1994–2004.

[11] Li, Y., Chen, X., and Li, N., "Online Optimal Control with Linear Dynamics and Predictions: Algorithms and Regret Analysis," *Adv. Neural Inf. Process. Syst.*, Vol. 32, edited by H. Wallach, H. Larochelle, A. Beygelzimer, F. d'Alché-Buc, E. Fox, and R. Garnett, 2019.

[12] Morgan, D., Subramanian, G. P., Chung, S.-J., and Hadaegh, F. Y., "Swarm Assignment and Trajectory Optimization using Variable-swarm, Distributed Auction Assignment and Sequential Convex Programming," *Int. J. Robot. Res.*, Vol. 35, No. 10, 2016, pp. 1261–1285.

[13] Miyato, T., Kataoka, T., Koyama, M., and Yoshida, Y., "Spectral Normalization for Generative Adversarial Networks," *Int. Conf. Learn. Representations*, 2018.

[14] Hewing, L., Wabersich, K. P., Menner, M., and Zeilinger, M. N., "Learning-based Model Predictive Control: Toward Safe Learning in Control," *Annu. Rev. Control Robot. Auton. Syst.*, Vol. 3, No. 1, 2020, pp. 269–296.

[15] Chung, S.-J., Ahsun, U., and Slotine, J.-J. E., "Application of Synchronization to Formation Flying Spacecraft: Lagrangian Approach," *J. Guid. Control Dyn.*, Vol. 32, No. 2, 2009, pp. 512–526.

[16] Tsukamoto, H., Chung, S.-J., and Slotine, J.-J. E., "Contraction Theory for Nonlinear Stability Analysis and Learning-based Control: A Tutorial Overview," *Annual Reviews in Control*, Vol. 52, 2021, pp. 135–169.

[17] Engelhardt, T., Jedicke, R., Vereš, P., Fitzsimmons, A., Denneau, L., Beshore, E., and Meinke, B., "An Observational Upper Limit on the Interstellar Number Density of Asteroids and Comets," *Astron. J.*, Vol. 153, No. 3, 2017, p. 133.

[18] Slotine, J.-J. E., and Li, W., *Applied Nonlinear Control*, Pearson, Upper Saddle River, NJ, 1991.

[19] Morari, M., and H. Lee, J., "Model Predictive Control: PAST, Present and Future," *Comput. Chem. Eng.*, Vol. 23, No. 4, 1999, pp. 667–682.

[20] Bemporad, A., and Morari, M., "Robust Model Predictive Control: A Survey," *Robustness in identification and control*, Springer London, London, 1999, pp. 207–226.

[21] Mayne, D. Q., Kerrigan, E. C., van Wyk, E. J., and Falugi, P., “Tube-based Robust Nonlinear Model Predictive Control,” *Int. J. Robust Nonlinear Control*, Vol. 21, No. 11, 2011, pp. 1341–1353.

[22] Lopez, B. T., Slotine, J.-J. E., and How, J. P., “Dynamic Tube MPC for Nonlinear Systems,” *Proc. Amer. Control Conf.*, 2019, pp. 1655–1662.

[23] Singh, S., Majumdar, A., Slotine, J.-J. E., and Pavone, M., “Robust Online Motion Planning via Contraction Theory and Convex Optimization,” *IEEE ICRA*, 2017, pp. 5883–5890.

[24] Singh, S., Tsukamoto, H., Lopez, B. T., Chung, S.-J., and Slotine, J.-J. E., “Safe Motion Planning with Tubes and Contraction Metrics,” *IEEE Conf. Decis. Control*, 2021, pp. 2943–2948.

[25] Carius, J., Farshidian, F., and Hutter, M., “MPC-Net: A First Principles Guided Policy Search,” *IEEE Robot. Automat. Lett.*, Vol. 5, No. 2, 2020, pp. 2897–2904.

[26] Everett, M., Chen, Y. F., and How, J. P., “Motion Planning Among Dynamic, Decision-making Agents with Deep Reinforcement Learning,” *IEEE/RSJ IROS*, 2018, pp. 3052–3059.

[27] Berkenkamp, F., Turchetta, M., Schoellig, A., and Krause, A., “Safe Model-based Reinforcement Learning with Stability Guarantees,” *Adv. Neural Inf. Process. Syst.*, Vol. 30, Curran Associates, Inc., 2017, pp. 908–918.

[28] Tsukamoto, H., and Chung, S.-J., “Learning-based Robust Motion Planning with Guaranteed Stability: A Contraction Theory Approach,” *IEEE Robot. Automat. Lett.*, Vol. 6, No. 4, 2021, pp. 6164–6171.

[29] Rivi  re, B., H  nig, W., Yue, Y., and Chung, S.-J., “GLAS: GLOBAL-to-local Safe Autonomy Synthesis for Multi-robot Motion Planning with End-to-end Learning,” *IEEE Robot. Automat. Lett.*, Vol. 5, No. 3, 2020, pp. 4249–4256.

[30] Rivi  re, B., H  nig, W., Anderson, M., and Chung, S.-J., “Neural Tree Expansion for Multi-robot Planning in Non-cooperative Environments,” *IEEE Robotics and Automation Letters*, Vol. 6, No. 4, 2021, pp. 6868–6875.

[31] STagliabue, A., Kim, D.-K., Everett, M., and How, J. P., “Demonstration-efficient Guided Policy Search via Imitation of Robust Tube MPC,” *IEEE ICRA*, Vol. to appear, 2022.

[32] Meech, K., “Setting the Scene: What Did We Know Before Rosetta?” *Philisophical Transactions of the Royal Society*, Vol. 375, No. 2097, 2017.

[33] Donitz, B., et al., “New Froniters Mission Concept Study to Explore Oort Cloud Comets,” *Community White Papers Planet. Sci. Decadal Surv.*, 2020.

[34] National Academies of Sciences, Engineering, and Medicine, *Origins, Worlds, and Life: A Decadal Strategy for Planetary Science and Astrobiology 2023-2032*, The National Academies Press, Washington, DC, 2022.

[35] Chang, I., Chung, S.-J., and Blackmore, L., “Cooperative Control with Adaptive Graph Laplacians for Spacecraft Formation Flying,” *IEEE Conf. Decis. Control*, 2010, pp. 4926–4933.

[36] Morgan, D., Chung, S.-J., Blackmore, L., Acikmese, B., Bayard, D., and Hadaegh, F. Y., “Swarm-keeping Strategies for Spacecraft under J_2 and Atmospheric Drag Perturbations,” *J. Guid. Control Dyn.*, Vol. 35, No. 5, 2012, pp. 1492–1506.

[37] Junkins, J. L., and Schaub, H., *Analytical Mechanics of Space Systems*, 2nd ed., AIAA, 2018.

[38] Chung, S.-J., Bandyopadhyay, S., Chang, I., and Hadaegh, F. Y., “Phase Synchronization Control of Complex Networks of Lagrangian Systems on Adaptive Digraphs,” *Automatica*, Vol. 49, No. 5, 2013, pp. 1148–1161.

[39] Bonnabel, S., and Slotine, J.-J. E., “A Contraction Theory-based Analysis of the Stability of the Deterministic Extended Kalman Filter,” *IEEE Trans. Autom. Control*, Vol. 60, No. 2, 2015, pp. 565–569.

[40] Dani, A. P., Chung, S.-J., and Hutchinson, S., “Observer Design for Stochastic Nonlinear Systems via Contraction-based Incremental Stability,” *IEEE Trans. Autom. Control*, Vol. 60, No. 3, 2015, pp. 700–714.

[41] Tsukamoto, H., and Chung, S.-J., “Neural Contraction Metrics for Robust Estimation and Control: A Convex Optimization Approach,” *IEEE Control Syst. Lett.*, Vol. 5, No. 1, 2021, pp. 211–216.

[42] Tsukamoto, H., Chung, S.-J., and Slotine, J.-J. E., “Neural Stochastic Contraction Metrics for Learning-based Control and Estimation,” *IEEE Control Syst. Lett.*, Vol. 5, No. 5, 2021, pp. 1825–1830.

[43] Nakka, Y. K., Hönig, W., Choi, C., Harvard, A., Rahmani, A., and Chung, S.-J., “Information-based Guidance and Control Architecture for Multi-spacecraft On-orbit Inspection,” *AIAA Scitech*, 2021.

[44] Darby, M. L., and Nikolaou, M., “MPC: Current Practice and Challenges,” *Control Eng. Pract.*, Vol. 20, No. 4, 2012, pp. 328–342.

[45] Foust, R., Chung, S.-J., and Hadaegh, F. Y., “Optimal Guidance and Control with Nonlinear Dynamics using Sequential Convex Programming,” *J. Guid. Control Dyn.*, Vol. 43, No. 4, 2020, pp. 633–644.

[46] Morgan, D., Chung, S.-J., and Hadaegh, F. Y., “Model Predictive Control of Swarms of Spacecraft using Sequential Convex Programming,” *J. Guid. Control Dyn.*, Vol. 37, No. 6, 2014, pp. 1725–1740.

[47] Schulman, J., Duan, Y., Ho, J., Lee, A., Awwal, I., Bradlow, H., Pan, J., Patil, S., Goldberg, K., and Abbeel, P., “Motion Planning with Sequential Convex Optimization and Convex Collision Checking,” *Int. J. Robot. Res.*, Vol. 33, No. 9, 2014, pp. 1251–1270.

[48] Boyd, S., and Vandenberghe, L., *Convex Optimization*, Cambridge University Press, 2004.

[49] Kloeden, P., and Rasmussen, M., *Nonautonomous Dynamical Systems*, Vol. 176, 2011.

[50] Robbins, H., and Monro, S., “A Stochastic Approximation Method,” *Ann. Math. Statist.*, Vol. 22, No. 3, 1951, pp. 400 – 407.

[51] Wensing, P. M., and Slotine, J.-J. E., “Beyond Convexity -- Contraction and Global Convergence of Gradient Descent,” *PLOS ONE*, Vol. 15, 2020, pp. 1–29.

[52] Bartlett, P. L., Foster, D. J., and Telgarsky, M. J., “Spectrally-normalized Margin Bounds for Neural Networks,” *Adv. Neural Inf. Process. Syst.*, Vol. 30, 2017.

[53] Neyshabur, B., Bhojanapalli, S., and Srebro, N., “A PAC-Bayesian Approach to Spectrally-normalized Margin Bounds for Neural Networks,” *Int. Conf. Learn. Representations*, 2018.

[54] Liu, A., Shi, G., Chung, S.-J., Anandkumar, A., and Yue, Y., “Robust Regression for Safe Exploration in Control,” *CoRL*, 2020.

[55] Chen, X., Monfort, M., Liu, A., and Ziebart, B. D., “Robust Covariate Shift Regression,” *19th Int. Conf. Artif. Intell. Statist.*, Proc. Mach. Learn. Res., Vol. 51, edited by A. Gretton and C. C. Robert, Cadiz, Spain, 2016, pp. 1270–1279.

[56] Chen, R. T. Q., Rubanova, Y., Bettencourt, J., and Duvenaud, D. K., “Neural Ordinary Differential Equations,” *Adv. Neural Inf. Process. Syst.*, Vol. 31, 2018.

[57] Tuor, A., Drgona, J., and Vrabie, D., “Constrained Neural Ordinary Differential Equations with Stability Guarantees,” arXiv:2004.10883, Apr. 2020.

[58] Dong, C., Liu, L., Li, Z., and Shang, J., “Towards Adaptive Residual Network Training: A Neural-ODE Perspective,” *37th Int. Conf. Mach. Learn.*, Proc. Mach. Learn. Res., Vol. 119, PMLR, 2020, pp. 2616–2626.

[59] Grunbacher, S., Hasani, R., Lechner, M., Cyranka, J., Smolka, S. A., and Grosu, R., “On the Verification of Neural ODEs with Stochastic Guarantees,” *Proc. AAAI Conf. Artif. Intell.*, Vol. 35, No. 13, 2021, pp. 11525–11535.

[60] Chen, H., Mo, Z., Yang, Z., and Wang, X., “Theoretical Investigation of Generalization Bound for Residual Networks,” *Proc. Int. Joint Conf. Artif. Intell.*, 2019, pp. 2081–2087.

[61] Biloš, M., Sommer, J., Rangapuram, S. S., Januschowski, T., and Günnemann, S., “Neural Flows: Efficient Alternative to Neural ODEs,” arXiv:2110.13040, Oct. 2021.

[62] Zakwan, M., Xu, L., and Ferrari-Trecate, G., “On Robust Classification using Contractive Hamiltonian Neural ODEs,” arXiv:2203.11805, Mar. 2022.

[63] Rodriguez, I. D. J., Ames, A. D., and Yue, Y., “LyaNet: A Lyapunov Framework for Training Neural ODEs,” arXiv:2202.02526, Feb. 2022.

[64] Jafarpour, S., Davydov, A., Proskurnikov, A., and Bullo, F., “Robust Implicit Networks via Non-Euclidean Contractions,” *Adv. Neural Inf. Process. Syst.*, Vol. 34, 2021, pp. 9857–9868.

[65] Jafarpour, S., Abate, M., Davydov, A., Bullo, F., and Coogan, S., “Robustness Certificates for Implicit Neural Networks: A Mixed Monotone Contractive Approach,” *Proc. Conf. Learn. Dyn. Control, To Appear*, 2022.

[66] Revay, M., Wang, R., and Manchester, I. R., “Recurrent Equilibrium Networks: Unconstrained Learning of Stable and Robust Dynamical Models,” *IEEE Conf. Decis. Control*, 2021, pp. 2282–2287.

[67] Manchester, I. R., Revay, M., and Wang, R., “Contraction-based Methods for Stable Identification and Robust Machine Learning: A Tutorial,” *IEEE Conf. Decis. Control*, 2021, pp. 2955–2962.

[68] Ames, A. D., Grizzle, J. W., and Tabuada, P., “Control Barrier Function Based Quadratic Programs with Application to Adaptive Cruise Control,” *IEEE Conf. Decis. Control*, 2014, pp. 6271–6278.

[69] Ames, A. D., Galloway, K., Sreenath, K., and Grizzle, J. W., “Rapidly Exponentially Stabilizing Control Lyapunov Functions and Hybrid Zero Dynamics,” *IEEE Trans. Autom. Control*, Vol. 59, No. 4, 2014, pp. 876–891.

[70] Khalil, H. K., *Nonlinear Systems*, 3rd ed., Prentice-Hall, Upper Saddle River, NJ, 2002.

[71] Kushner, H. J., *Stochastic Stability and Control*, Academic Press New York, 1967.

[72] Geoffrey R. Grimmett, D. S., *Probability and Random Processes*, 3rd ed., Oxford University Press, United Kingdom, 2001.

[73] Tsukamoto, H., and Chung, S.-J., “Robust Controller Design for Stochastic Nonlinear Systems via Convex Optimization,” *IEEE Trans. Autom. Control*, Vol. 66, No. 10, 2021, pp. 4731–4746.

[74] Lohmiller, W., and Slotine, J.-J. E., “On Contraction Analysis for Nonlinear Systems,” *Automatica*, Vol. 34, No. 6, 1998, pp. 683 – 696.

[75] Manchester, I. R., and Slotine, J.-J. E., “Control Contraction Metrics: Convex and Intrinsic Criteria for Nonlinear Feedback Design,” *IEEE Trans. Autom. Control*, Vol. 62, No. 6, 2017, pp. 3046–3053.

[76] Chung, S.-J., “Nonlinear Control and Synchronization of Multiple Lagrangian Systems with Application to Tethered Formation Flight Spacecraft,” Ph.D. thesis, MIT, 2007.

[77] Tsukamoto, H., Chung, S.-J., Slotine, J.-J., and Fan, C., “A Theoretical Overview of Neural Contraction Metrics for Learning-based Control with Guaranteed Stability,” *IEEE Conf. Decis. Control*, 2021, pp. 2949–2954.

[78] Han, S., and Chung, S.-J., “Incremental Nonlinear Stability Analysis for Stochastic Systems Perturbed By Lévy Noise,” arXiv:2103.13338, Mar. 2021.

[79] Nakka, Y. K., and Chung, S.-J., “Trajectory Optimization of Chance-constrained Nonlinear Stochastic Systems for Motion Planning and Control,” *IEEE Trans. Robot.*, Vol. to appear, 2022.

[80] Arnold, L., *Stochastic Differential Equations: Theory and Applications*, Wiley, 1974.

[81] Slotine, J.-J. E., Wang, W., and El Rifai, K., “Contraction Analysis of Synchronization in Networks of Nonlinearly Coupled Oscillators,” *Int. Symp. Math. Theory Netw. Syst.*, 2004.

[82] Lohmiller, W., and Slotine, J.-J. E., “Nonlinear Process Control using Contraction Theory,” *AIChE Journal*, Vol. 46, 2000, pp. 588 – 596.

[83] Pham, Q., “Analysis of Discrete and Hybrid Stochastic Systems By Nonlinear Contraction Theory,” *Int. Conf. Control Autom. Robot. Vision*, 2008, pp. 1054–1059.

[84] Tsukamoto, H., and Chung, S.-J., “Convex Optimization-based Controller Design for Stochastic Nonlinear Systems using Contraction Analysis,” *IEEE Conf. Decis. Control*, 2019, pp. 8196–8203.

[85] Wang, R., Tóth, R., and Manchester, I. R., “Discrete-time Contraction-based Control of Nonlinear Systems with Parametric Uncertainties using Neural Networks,” arXiv:2105.05432, May 2021.

[86] Tsukamoto, H., Chung, S.-J., and Slotine, J.-J. E., “Learning-based Adaptive Control using Contraction Theory,” *IEEE Conf. Decis. Control*, 2021, pp. 2533–2538.

[87] Lopez, B. T., and Slotine, J.-J. E., “Universal Adaptive Control of Nonlinear Systems,” *IEEE Control Systems Lett.*, Vol. 6, 2022, pp. 1826–1830.

[88] Nakka, Y. K., Liu, A., Shi, G., Anandkumar, A., Yue, Y., and Chung, S.-J., “Chance-constrained Trajectory Optimization for Safe Exploration and Learning of Nonlinear Systems,” *IEEE Robot. Automat. Lett.*, Vol. 6, No. 2, 2021, pp. 389–396.

[89] Boffi, N. M., Tu, S., and Slotine, J.-J. E., “Regret Bounds for Adaptive Nonlinear Control,” *Proc. Conf. Learn. Dyn. Control, Proc. Mach. Learn. Res.*, Vol. 144, 2021, pp. 471–483.

[90] Shi, G., Azizzadenesheli, K., O' Connell, M., Chung, S.-J., and Yue, Y., “Meta-adaptive Nonlinear Control: Theory and Algorithms,” *Adv. Neural Inf. Process. Syst.*, Vol. 34, 2021, pp. 10013–10025.

[91] Kakade, S., Krishnamurthy, A., Lowrey, K., Ohnishi, M., and Sun, W., “Information Theoretic Regret Bounds for Online Nonlinear Control,” *Adv. Neural Inf. Process. Syst.*, Vol. 33, 2020, pp. 15312–15325.

[92] Paszke, A., Gross, S., Massa, F., Lerer, A., Bradbury, J., Chanan, G., Killeen, T., Lin, Z., Gimelshein, N., Antiga, L., Desmaison, A., Kopf, A., Yang, E., DeVito, Z., Raison, M., Tejani, A., Chilamkurthy, S., Steiner, B., Fang, L., Bai, J., and Chintala, S., “PyTorch: An Imperative Style, High-performance Deep Learning Library,” *Adv. Neural Inf. Process. Syst.*, Vol. 32, Curran Associates, Inc., 2019.

[93] Acton, C. H., “Ancillary Data Services of NASA’s Navigation and Ancillary Information Facility,” *Planet. Space Sci.*, Vol. 44, No. 1, 1996, pp. 65–70.

[94] Acton, C., Bachman, N., Semenov, B., and Wright, E., “A Look Towards the Future in the Handling of Space Science Mission Geometry,” *Planet. Space Sci.*, Vol. 150, 2018, pp. 9–12.